DESIGN AND SIMULATION OF STRAIGHT AND TILTED HELICAL COILS FOR MAGNETIC RESONANCE IMAGING

by

M. Zahid Sağıroğlu

B.S., Electrical and Electronics Engineering, Boğaziçi University, 2012

Submitted to the Institute for Graduate Studies in
Science and Engineering in partial fulfillment of
the requirements for the degree of
Master of Science

Graduate Program in Electrical and Electronics Engineering
Boğaziçi University

2015

ACKNOWLEDGEMENTS

It is a priceless gift that working with understanding and helpful people. I had this gift during my thesis study, thanks to all those wonderful people around.

I would like to start with my supervisor, Assoc. Prof. Şenol Mutlu. I am very pleased to work with him for all these years, and experience his patience and constructive guidance. Another person I would like to name here is Asst. Prof. Özgür Kocatürk, my co-supervisor, for his invaluable perspective and contribution to this dissertation.

I want to thank Engin Baysoy. He added this study a lot with not only his academical skills, but also his positive attitude. I also thank Korel Yıldırım for his determination which motivated our team to achieve the goals of this project.

I would like to thank Ergin Dinç, who is always ready to help with his brilliant mind and strong analytical skills. I also would like to mention the names of Ozan Ertop and Emre İşeri here. They always make the time that I spend in the laboratory valuable. I'd also like to thank my dearest friends İlteber Kaan Keleş, Serhat İşcan and Alim Vedat Süner for their patience and tolerance especially through the end of this thesis study, and Said Altuner for his substantial support.

Finally, I owe my greatest gratitude to my family, for their never-ending both moral and material support. I especially want to thank Semih Sağıroğlu, my brother, for being a valuable flatmate, an irreplaceable friend, and a ministrant elder brother.

This thesis is carried out as a part of the research project which is supported by TUBITAK (Scientific and Technical Research Council of Turkey) under Contract 112R024. And I want to thank BİDEB-2210 program of TUBITAK for their financial contribution to my graduate studies.

ABSTRACT

DESIGN AND SIMULATION OF STRAIGHT AND TILTED HELICAL COILS FOR MAGNETIC RESONANCE IMAGING

In this thesis, helical coils are studied through Finite Element Method (FEM) analysis and fabrications are done as a part of the project of 5 Fr guiding catheter design for paediatric intracardiac procedures performed under Magnetic Resonance Imaging (MRI). The aim is to provide a reliable method to test the designed receiver coil structures without the need for fabrication. Straight and tilted helical coils are studied in details in order to bring out comparison between different models of helical coils which can be used for MRI applications. The mathematical expressions of these helices are pointed out and their magnetic flux densities are stated via dipole design methodology. FEM simulations are carried out for sample helical coils to make the computational analysis of their electrical and magnetic characteristics. After this, straight and tilted helical coils are fabricated having 10 mm and 5 mm diameter with changing winding numbers. These 26 fabricated coils are characterized via a vector network analyzer. The results are discussed to show the reliability of FEM simulations for their usage in catheter LC tip designs. Finally, a concept design and simulations of 1.5T MRI catheter device with double helical coils are performed using the same methodology, and the resonance frequency is found approximately as 63 MHz. The MRI test of a fabricated LC resonator circuit on catheter, which is carried out in parallel to this thesis study as a part of the overall project, is introduced in future works, aiming to combine FEM simulations and Micro Electro Mechanical Systems (MEMS) fabrication methods to produce optimized LC circuits for catheters.

ÖZET

MANYETİK REZONANS GÖRÜNTÜLEME İÇİN DÜZ VE EĞİMLİ HELEZON BOBİNLERİN TASARIMI VE SİMULASYONU

Bu tezde, Manyetik Rezonans Görüntüleme (MRG) altında gerçekleştirilen pediatrik kalp içi operasyonlar için 5 Fr kılavuz kateter geliştirilmesi projesi kapsamında, Sonlu Öge Metodu (SÖM) yöntemiyle helezon bobinler çalışılmıştır. Amaç, tasarlanan bobin yapılarını üretmeden test etmek için güvenilir bir yöntem ortaya koymaktır. MRG uygulamalarında kullanılabilecek farklı tipteki helezon bobin modellerinin karşılaştırılması amacıyla düz ve eğimli helezon bobinler çalışılmıştır. Bu helezon yapılarının matematiksel tanımlamaları belirtilmiş ve dipol hesaplaması yöntemiyle manyetik akı yoğunlukları gösterilmiştir. Bobin örneklerinin elektriksel ve manyetik özelliklerinin analiz edilebilmesi amacıyla farklı SÖM simulasyonları gerçekleştirilmiştir. Bunu takiben, 10 mm ve 5 mm çaplarına sahip, değişken sarmal sayılarda düz ve eğimli helezon bobinler üretilmiştir. Üretilen bu 26 bobin bir ağ çözümleyici aracılığıyla test edilmiştir. Elde edilen tüm sonuçlar, LC katater ucu modellemelerinde SÖM simülasyonlarının güvenilirliği ortaya koymak için değerlendirilmiştir. Son olarak, aynı yöntem kullanılarak çifte eğimli helezon bobin yapısı içeren 1.5T MRG kateter cihazının konsept tasarım ve simulasyonları gerçekleştirilmiş ve rezonans frekansı yaklaşık 63 MHz olarak tespit edilmiştir. Bu tez çalışması paralelinde ana projenin bir parçası olarak devam ettirilen kateter üzerinde şekillendirilen LC rezonatör devresinin MRG testi, SÖM simulasyonlarını ve MEMS üretim metodlarını birleştirerek optimize edilmiş kateter yapıları tasarlamayı hedefleyen gelecek çalışmalar kapsamında ifade edilmiştir.

TABLE OF CONTENTS

ACKNOWLEDGEMENTS . . . iii
ABSTRACT . . . iv
ÖZET . . . v
LIST OF FIGURES . . . viii
LIST OF TABLES . . . xii
LIST OF SYMBOLS . . . xiii
LIST OF ACRONYMS/ABBREVIATIONS . . . xv
1. INTRODUCTION . . . 1
1.1. Catheterization and Imaging in Congenital Cardiac Diseases . . . 2
1.1.1. Interventional Imaging with Fluoroscopy . . . 3
1.1.2. Interventional Imaging with MRI . . . 4
1.2. Objective and Novelty . . . 4
1.3. Thesis Outline . . . 6
2. THEORY . . . 8
2.1. Catheter Devices for Interventional MRI . . . 8
2.2. Passive Devices . . . 8
2.2.1. Inductively Coupled (Semi Active) Devices . . . 9
2.2.2. Active Devices . . . 9
2.3. Coil Design for MR Detection . . . 11
2.3.1. Dipole Characteristics and Geometry of Helical Coils . . . 12
2.3.2. Straight Helical Coils . . . 14
2.3.3. Tilted Helical Coils . . . 15
2.3.4. Double Tilted Helical Coils . . . 16
3. DESIGN AND SIMULATION OF HELICAL COILS . . . 19
3.1. Design . . . 19
3.2. FEM Simulations . . . 21
3.2.1. 3D Design Transfer and Mesh Creation . . . 22
3.2.2. Magnetic Field Studies . . . 24
3.2.2.1. Inductance Calculations . . . 24

3.2.2.2. Magnetic Fields and Frequency Response 26
3.2.3. Resonance Frequency Derivation 31
3.2.4. Electromagnetic Waves – Frequency Response 32
4. FABRICATIONS AND MEASUREMENTS 35
4.1. Inductor Fabrication 35
4.1.1. Design and Fabrication of Template Plastic Core 35
4.1.2. Fabrication of Tilted and Straight Helical Coils 37
4.2. Measurement Setup and Calibration 39
4.2.1. Calibration of Network Analyzer 39
4.2.2. Inductance Measurement Method 40
4.2.2.1. Design and Fabrication of Non-Contact Search Probe . 41
4.3. Measurements of Tilted and Straight Helical Coils 43
4.3.1. Tilted Helical Coils 43
4.3.1.1. Observed Effects of Diameter Change for Tilted Coils . 45
4.3.2. Straight Helical Coils 48
4.3.2.1. Observed Effects of Diameter Change for Straight Coils 50
4.3.3. Comparison of Tilted and Straight Helical Coils Measurements and Directivity 53
4.4. Comparison of Simulations and Measurements 55
5. MRI RECEIVER COIL DESIGN FOR 5 FR CATHETER 57
5.1. Geometry and Circuit Modelling 57
5.1.1. Circuit Modelling 58
5.1.2. Ring Capacitor 60
5.1.3. Intermediary Capacitor 61
5.1.4. Overlap Capacitor 62
5.1.5. Tilted Helical Coils 63
5.2. HFSS Simulations 64
6. CONCLUSION AND FUTURE WORK 68
REFERENCES 72

LIST OF FIGURES

Figure 2.1. In vivo images acquired with stents implanted into the right renal artery and the splenic artery of a pig [12]. 10

Figure 2.2. Three representative approaches to catheters designed to be tracked using cardiovascular magnetic resonance (CMR) [19]. 11

Figure 2.3. 3D representation of straight helix. 15

Figure 2.4. 3D representation of tilted helix. 16

Figure 2.5. 3D representation of double tilted helix. 17

Figure 2.6. Magnetic flux densities of each helix in double tilted helix. 18

Figure 3.1. Thickness measurement of copper wire via microscope. 19

Figure 3.2. 3D design of a coil. 20

Figure 3.3. Meshed coil structure in the simulation model. 22

Figure 3.4. Closer image of created meshes for winding and plastic core. . . . 23

Figure 3.5. Simulated inductance values of tilted helical coils with 10 mm diameter. 25

Figure 3.6. Inductance values of all simulated helical coils. 26

Figure 3.7. Magnetic flux density stream lines for tilted helical coil. 27

Figure 3.8. Magnetic field norm plot of tilted helical coil. 28

Figure 3.9. Plane dependent magnetic field norm plots tilted helical coil. . . . 28

Figure 3.10. Frequency dependent magnetic field norm plots tilted helical coil. . 30

Figure 3.11. Lumped port impedance change with frequency for 8.5 turn tilted helical coil with 10 mm diameter. 30

Figure 3.12. Electric field plot of 8.5 turn tilted helical coil with 10 mm diameter. 32

Figure 3.13. Far field plot of 8.5 turn tilted helical coil with 10 mm diameter. . 33

Figure 3.14. The plot of S_{11} for 8.5 turn tilted helical coil with 10 mm diameter. 33

Figure 4.1. 3D design of template plastic core for tilted helices. 36

Figure 4.2. Fabricated coils with models. 37

Figure 4.3. Fabricated straight helical coils of 5 mm and 10 mm diameters with changing turn numbers. 38

Figure 4.4. Smith chart caption of 50 Ω resistor measurement. 40

Figure 4.5. Excitation of the test inductor in the LC circuit by the magnetic field generated by the measurement coil. 41

Figure 4.6. Measurement preparations. 42

Figure 4.7. Assembled LC circuits with coils and 820 pF ceramic capacitance. 43

Figure 4.8. Resonance frequency caption for 8.5 turn and 10 mm diameter coil. 44

Figure 4.9. Measured inductance values for 10 mm diameter tilted helical coils. 45

Figure 4.10. Measured inductance values of tilted helical coils. 46

Figure 4.11. Resonance frequency caption for 6.5 turn 10 mm tilted helical coil. 47

Figure 4.12. Resonance frequency caption of 6.5 turn 5 mm tilted helical coil. . 48

Figure 4.13. Resonance frequency caption of 8.5 turn 10 mm straight helical coil via vector network analyzer. 49

Figure 4.14. Measured inductance values for 10 mm diameter straight helical coils. 50

Figure 4.15. Measured inductance values of straight helical coils. 51

Figure 4.16. Resonance frequency caption of 6.5 turn 10 mm straight helical coil. 52

Figure 4.17. Resonance frequency caption of 6.5 turn 5 mm straight helical coil. 52

Figure 4.18. Complete measured inductance values of coils. 53

Figure 4.19. Directionality captions of tilted and straight helical coils. 54

Figure 4.20. Inductance results of simulations and measurements. 55

Figure 4.21. Directionality simulations of tilted and straight helical coils. 56

Figure 5.1. Designed double helix catheter structure for MRI. 58

Figure 5.2. Structural elements of the double helix resonator. 59

Figure 5.3. Electrical model of the catheter device. 59

Figure 5.4. Simplified electrical model of the catheter device. 60

Figure 5.5. Ring capacitor. 61

Figure 5.6. Intermediary capacitor. 62

Figure 5.7. Overlap capacitor. 63

Figure 5.8. Tilted helices. 64

Figure 5.9. Magnetic field inside the geometry. 65

Figure 5.10. Magnetic field around the catheter. 65

Figure 5.11. S_{11} plot of the structure. 66

Figure 5.12. Inductance plot near resonance frequency. 67

Figure 6.1. LC resonator structure fabricated on 5 Fr catheter. 69

Figure 6.2. MR image of the fabricated LC resonator. 70

LIST OF TABLES

Table 4.1. Test Measurement Results. 42

LIST OF SYMBOLS

A	Area of plates of capacitor
B	Magnetic Flux Density
C	Capacitance
C_{coil}	Self capacitance of inductor
C_{int}	Intermediary capacitor
$C_{overlap}$	Overlap capacitor
C_{ring}	Ring capacitor
d	Separation between two planes of capacitor
dB	Decibel, logarithmic unit
$D_{cylinder}$	Diameter of core cylinder of inductor
f_c	Center frequency
fF	Femto-farads, capacitance unit
Fr	French, catheter scale
GHz	Giga-hertz, frequency unit
H	Magnetic Field
I	Current
L	Inductance
L_{inner}	Inner tilted helix inductor
L_{outer}	Outer tilted helix inductor
MHz	Mega-hertz, frequency unit
mm	Milli-meters, metric unit
mm^2	Area in metric system
N	Number of turns for coils
nH	Nano-henries, inductance unit
fF	Pico-farads, capacitance unit
$Port_1$	Excitation port
$Port_2$	Excitation port
R	Resistance

R_{coil}	Self resistance of inductor
r_{mean}	Mean radius for curvature of capacitor pads
S_{11}	Input port voltage reflection coefficient
$t_{insulator}$	Insulator thickness
t_{wire}	Wire thickness
ϕ	Magnetic flux
ε	Electromotive force
ϵ_0	Permittivity of vacuum
ϵ_r	Relative permittivity
Δf	Frequency range
Ω	Ohm, resistance unit
μ_0	Permeability of free space
μm	Micro-meters, metric unit

LIST OF ACRONYMS/ABBREVIATIONS

2D	Two Dimensional
3D	Three Dimensional
AC	Alternative Current
CMR	Cardiovascular Magnetic Resonance
CO_2	Carbon Dioxide
DC	Direct Current
FOV	Field of View
FISP	Fast Imaging with Steady State Precision
HFSS	High Frequency Structure Simulator
IED	Infinite Elements Domain
MEMS	Micro Electro Mechanical Systems
MR	Magnetic Resonance
MRI	Magnetic Resonance Imaging
NMR	Nuclear Magnetic Resonance
PML	Perfectly Matched Layer
RF	Radio Frequency
SMA	SubMiniature version A
SNR	Signal to Noise Ratio
STC	Single Turn Coil
VSWR	Voltage Standing Wave Ratio

1. INTRODUCTION

Imaging of human internal organs with exact and non-invasive methods is very important for medical diagnosis, treatment and follow-up. Researches have being carried out in order to create better methodologies and techniques for this purpose. In 1970s the studies based on the principles of Nuclear Magnetic Resonance (NMR) and other physical techniques were carried out, and different methods were developed on that to be used for body imaging purposes. In 1972, Paul Laterbur discovered the possibility of creating two-dimensional images by introducing gradients in the magnetic field [1]. The idea was detecting the origins of gradients by analyzing the characteristics of the emitted radio waves. This method made it possible to build up two-dimensional pictures of structures that could not be visualized with other methods back then. Only two years later, the first 3-dimensional imaging method was explained by Peter Mansfield who further developed the utilization of gradients in the magnetic field, and showed how the signals could be mathematically analyzed, which made it possible to develop a useful imaging technique [2], Magnetic Resonance Imaging (MRI) was introduced.

As a result of continuing research studies over years, MRI has been transformed into a convenient tool for physiological imaging and medical treatment. In addition to all advantages introduced by MRI to medical studies, the interventional imaging with MRI in congenital cardiac diseases of paediatric patients is stated out as one of the most merging fields [3–7]. Fluoroscopy is one of the main techniques which is used interventions in congenital cardiac diseases. However, exposing to ionizing radiation results in increased cancer risk for the young paediatric patients [8]. MRI is a good candidate at this point being lack of ionizing radiation.

In order to turn MRI into a widely used method for treatment of congenital cardiac diseases by using interventional catheterization, associated tools have to be created to increase the success rate of the procedures. One of the most important tools in this perspective is catheter which is used during interventions to perform the operation. And designing an MRI compatible and safe catheter for paediatric patients

is considerably challenging issue due to the combination of electrical and mechanical requirements and profile constraints. The project, which includes this thesis study as a part of itself, aims to design and fabricate convenient catheter devices for localization under MR imaging of interventional congenital cardiac diseases.

1.1. Catheterization and Imaging in Congenital Cardiac Diseases

The human heart already fully developed between the eighth and tenth weeks after conception and any congenital abnormalities are already present. Multiple factors, including genetic and environmental ones, may cause the malformation of the heart during this period such as exposure to certain medications, viruses, parasites, metabolic disorders (such as uncontrolled diabetes), and excessive alcohol consumption.

Forms of congenital heart disease incorporate ventricular septal defects and atrial septal defects that infant have an opening in the atrioventricular septum, pulmonic and aortic stenosis that the pulmonic or aortic valves are narrower than normal, coarctation (narrowing) of the aorta that the aorta is pinched or narrowed after it leaves the heart, and holes in the inner, separating walls of the heart that allow blood to leak or flow directly from one chamber or artery into another rather than flowing in the proper sequence through the valves. In past for all these congenital defects physician call for surgery. However, catheter based invasive approaches for adults have been preferred against surgical procedures recently due to the reduction of operation time, patient discomfort, hospitalization time, and procedure related risks.

Catheterization method involves inserting a small diameter cardiac catheter (flexible tube) into a vein or artery and then steering it into various cardiac chambers and blood vessels by the assistance of medial equipment images. The image creation may rely on different techniques at this point such as fluoroscopy or MRI. Each technique brings unique advantages and disadvantages from the view of fabrication of used catheter, ease of monitoring and possible side effects. Comparing those positive and negative contributions of imaging techniques, MRI stands out more suitable for imaging of paediatric cardiovascular interventions due to its ionizing radiation free mechanism.

1.1.1. Interventional Imaging with Fluoroscopy

Fluoroscopic images are moving radiographic images displayed on a monitor which exploit ionizing radiation to generate images of the human body. During the procedure in order to enhance the visibility and tracking of intravascular devices, a radiopaque dye (barium solution) injection is applied through the patient's vessel while the body is under frequent X-ray exposures.

Although X-ray fluoroscopy is widely used as an imaging modality for the minimally invasive procedures, it suffers from poor soft tissue contrast and requires assumptions on device position and orientation based on anatomic landmarks which may be inaccurate. X-ray fluoroscopy merely provides luminographic data without insight into vessel wall structure and underlying plaque morphology. These data. However, are believed to be crucial for determining the origin of intimal proliferation and thus for the outcome of vascular interventions [9–12].

Furthermore, x-ray exposures consist of ionizing radiation that has enough energy to potentially cause damage to DNA and may elevate a person's lifetime risk of developing cancer. It's known that even to be exposed to radiation for a short period of time increases the potential of cancer in later on [13]. Although radiation dose for a single procedure might be low, pediatric patients often receive repeated examinations over time to evaluate their conditions, which could result in relatively high cumulative doses.

Most important, children are considerably more sensitive to the carcinogenic effects of ionizing radiation than adults, and children have a longer life expectancy resulting in a larger window of opportunity for expressing radiation damage [8]. Moreover, fluoroscopy can result in relatively high radiation doses, especially for interventional procedures which require fluoroscopy be administered for a long period of time. A study showed that pediatric cardiac catheterization can induce, both acutely and in the long term, increased chromosomal DNA damage in circulating lymphocytes, which represents an intermediate end point of cancer [14].

1.1.2. Interventional Imaging with MRI

Over the last 10 years, significant advances in magnetic resonance imaging (MRI) technology and potential for complete multi planar soft tissue imaging and immediate functional assessment during cardiac intervention makes MRI extremely promising candidate to replace fluoroscopy. Image-guided catheter intervention on real-time imaging [3–7] and patient-handling [15] capabilities have been demonstrated. Nevertheless, clinical-grade interventional catheter devices for use during MR, such as catheters and guidewires, remain the most significant obstacle to wider clinical translation. Current non-clinical implementations tend to offer reduced visibility under MR or excessive size and reduced mechanical performance [16].

There is no known harm [17] of MRI when used within well-defined technical constraints [18]. The therapeutic use of MRI in cardiovascular procedures provides superior soft tissue contrast while eliminating the ionization radiation exposure on both patient and operator [19]. MRI also provides multi slice imaging and allows physiological measurements such as blood flow, temperature, perfusion and motion. The feasibility of endovascular interventional procedures such as renal artery stenosis treatment [20], abdominal aortic aneurysms treatment [21], recanalization of carotid chronic total occlusion [22], atrial septal puncture [23] and transcatheter aortic valve implantation [24] and electrophysiology mapping for atrial fibrillation treatment [25–27] have been successfully tested on animal models under magnetic resonance imaging.

1.2. Objective and Novelty

The use of MRI technique in interventional paediatric congenital cardiac diseases is a recent concept. Therefore, development of advance and convenient tools is a big necessity, and multiple researches are being carried out to improve the existing devices for imaging. Different structures such as micro solenoids or saddle coils have been studied as tracking devices for similar applications [28, 29]. Although there are multiple microcoil structures for MRI applications, this thesis study focuses on helical coil structures to indicate their advantages and availability for MRI applications.

The aim of this project is to design and fabricate proper catheter devices for the interventional procedures with MRI. Achieving this goal with expected influence requires combination of broader perspectives and methodologies. Carrying out fabrications without being certain of the design of subject results in time and effort loss since it is almost slim chance to bring out the perfect design at the initial trials. Therefore, a reliable method is needed to design the optimized catheter receiver structures, prior to fabrication steps.

Introducing a reliable method for designing catheter receiver structures is the main objective of this thesis study. For this purpose, simulation tools which depends on Finite Element Method (FEM) were considered as the objective platforms to bring out design methodology. Therefore, FEM simulations are aimed to be performed on sample structures which were also fabricated to point out the consistency of the tested approach.

During the thesis study, straight and tilted helical coils are chosen as objective samples, which are also candidate inductor parts for catheter receivers. Those sample coils are also aimed to be fabricated, in order to measure their characteristics via vector network analyzer. The results of simulations and fabrications are compared to indicate the reliability of the FEM simulations to design catheter tips for MRI applications. Once the consistency of the simulation method is confirmed, an initial 5 Fr catheter tip design and its simulations is planned to be performed. The design is aimed to include double tilted helical coil design as catheter tip, which will be a novel device if the fabrication process can be improved to carry out this multi-layer tilted designs.

Together with this thesis, which aims to set FEM simulations as design tools, fabrication methods of catheter devices were also studied and a proper and convenient technique was set to create the designed catheter devices by the other members of our team.

1.3. Thesis Outline

Up to this point in Chapter 1, the imaging methods for interventions of congenital cardiac diseases were discussed. The advantages and disadvantages of fluoroscopy and MRI was investigated in this perspective. The ionizing radiation free mechanism of MRI brings a considerable advantage to reduce down the risk of cancer for patients. At this point the objectives of this thesis study and overall project are revealed as bringing out proper methods to design and simulate catheter devices, and fabricating novel designs for the interventions congenital cardiac diseases with MRI.

In Chapter 2, the catheter device types, and their working principles are presented. The Ampere's Law and Faraday's Law for electromagnetism were described following that to make explain the background of dipole design of coils. The geometries of straight, tilted and double tilted helices are stated mathematically, and the magnitude and directionalities of their magnetic flux densities are represented.

Chapter 3 provides the carried out simulations for straight and tilted helical coils with changing dimensional values. The methods of creating 3D structures prior to simulations, structure modeling, parameter definition, material assignment and mesh creation are presented as compulsory steps before running simulations. Radio Frequency and AC/DC tools of FEM simulator program are used to solve related physics of coil structures. Stationary and frequency sweep analyzes are performed, and eigenvalues are obtained to disclose the characteristics of subject coils. 3D and surface plots of magnetic and electric fields are created as well as magnetic flux density contours. Results of simulations are compared in order to analyze the characteristics and differentiation aspects of straight and helical coils.

26 different coils were fabricated with the same dimensional parameters of the simulated coils in Chapter 4. Core objects for coil windings are designed and 3D printed out of plastics as templates. Assembling a standard ceramic capacitor to fabricated helical coils, LC resonator structures are formed. Via the non-contact search probe prepared for vector network analyzer, one port measurements were carried out. The

inductor values were extracted out from the observed resonance frequencies since the value of the capacitor was already known. Magnetic field directionalities of coils are also stated as well as the parameter dependencies of their inductance values. The results of simulation and fabrication steps are also compared to observe the reliability of the FEM simulations.

In Chapter 5, an MRI coil receiver design with double helical coils for 5 Fr catheter is introduced. Double helical windings on top of each other together with interlayer capacitors are designed for 1.5 T MRI. The structure was simulated via HFSS program, to observe the resulted electrical and magnetic characteristics. Related plots are generated to further study this initial catheter tip design.

In Chapter 6, the document is concluded with a brief summary of the achieved work in the thesis. The results of the fabrication studies of the overall project which are carried out by the other researchers in the project in parallel to this thesis study was briefly explained. The fabricated LC resonator is presented, together with the measurements and MRI test results. The future works of the projects which combine the simulation and fabrication steps to design and create catheter devices for MRI are presented as closure.

2. THEORY

2.1. Catheter Devices for Interventional MRI

Since MR imaging is based on different technology interventional MRI has the potential as an ionizing radiation-free alternative to conventional X-ray guided catheterization. But MRI has been used for diagnostic purpose in clinical settings so far due to lack of safe and conspicuous catheter devices. Engineering safe and conspicuous MRI catheters is especially challenging because of the combination of electrical and mechanical requirements and profile constraints. Interventional cardiovascular devices in MRI typically classified by the visualization mechanism called as passive, semi-active (inductively coupled) and active.

2.2. Passive Devices

Passive devices rely on intrinsic material properties for visibility during cardiac magnetic imaging (CMRI). Material magnetic susceptibility, or how it responds to a magnetic field, can cause inhomogeneities in the main magnetic field that result in signal voids (negative contrast or dark spots) on images. Positive contrast (bright spots) can be generated by the use of paramagnetic T1 shortening contrast agents [30]. The ferromagnetic [31], paramagnetic [32] or other approaches include filling catheter balloons with CO_2, in Figure 2.2, [33] or more novel contrast agent materials, such as 19F Fluorine, [34] are used to improve device visibility. Off-resonance imaging techniques [35, 36] improve the specificity of the device-related signal but usually sacrifice visibility of surrounding anatomy. Recently, non-metallic conspicuous guidewires have been developed that consist of small metal (susceptibility) markers, mimic the mechanical properties of metallic X-ray guidewires [37, 38].

Passive devices simpler to manufacture, avoid many of the radio frequency (RF) safety concerns. It is possible that the passive design preserve all desired mechanical properties while RF heating is not greater than 1^0C [39]. However, they remain difficult

to discern from background tissue in vivo, especially within curved vascular structures [19]. Beside that the appearance of the susceptibility artefact is influenced by deflection and by orientation. For example, when the tip is deflected perpendicular to the main magnetic field, the artefact is large and blurry [39]. And it may be difficult for the operator to visualize the exact location of the catheter tip.

2.2.1. Inductively Coupled (Semi Active) Devices

Semi active devices incorporate circuit elements such as inductively coupled markers [19]. Wireless inductive coupled devices (catheters) act as local RF signal amplifier [12] whose signal could be coupled to outside surface coils. These do not require long transmission lines (connecting electrical cables) and need not be connected directly to the scanner but may be more visible than passive devices. There are some different type of catheter tip designs experienced in semi active devices such as single loop, Gianturco, helix, and solenoid [19].

In transmit mode, detuning of RF resonators (passive decoupling) limits RF energy deposition in the catheter resonators which provides RF safety and broadens the range of applications [40]. However, device visualization of inductively coupled devices are limited to the distal tip of the catheters that contains markers [41, 42]. Further optical tuning [43, 44] or signal separation [45] techniques may be required to clearly distinguish these devices from background imaging.

2.2.2. Active Devices

Active devices incorporate small coils or antennae connected to the scanner on separate channels through long transmission lines for device tracking or profiling purpose [46]. Tracking requires special cardiovascular MR sequences to locate the tracking coil in 3D space with the computer-synthesized device position overlaid onto image which can be seen in Figure 2.2. Clinical-grade active guidewires and catheters are nearing clinical reality [47], but thorough performance and safety evaluation remains an important step [19].

Since long, metallic components have the potential for heating during MRI radio frequency (RF) excitation [39], MRI compatible materials and instruments have to be used during construction of dedicated interventional MRI devices.

Clinical grade active endovascular catheters and guidewires are nearing clinical reality [48], but before moving on clinical trials, the radio frequency (RF) induced heating risk over long conductor components of the devices needs to be addressed. The pulsed electromagnetic RF field (B1) may induce currents over long conductors in intravascular devices and cause heating especially near the device tips [49] due to resistive losses.

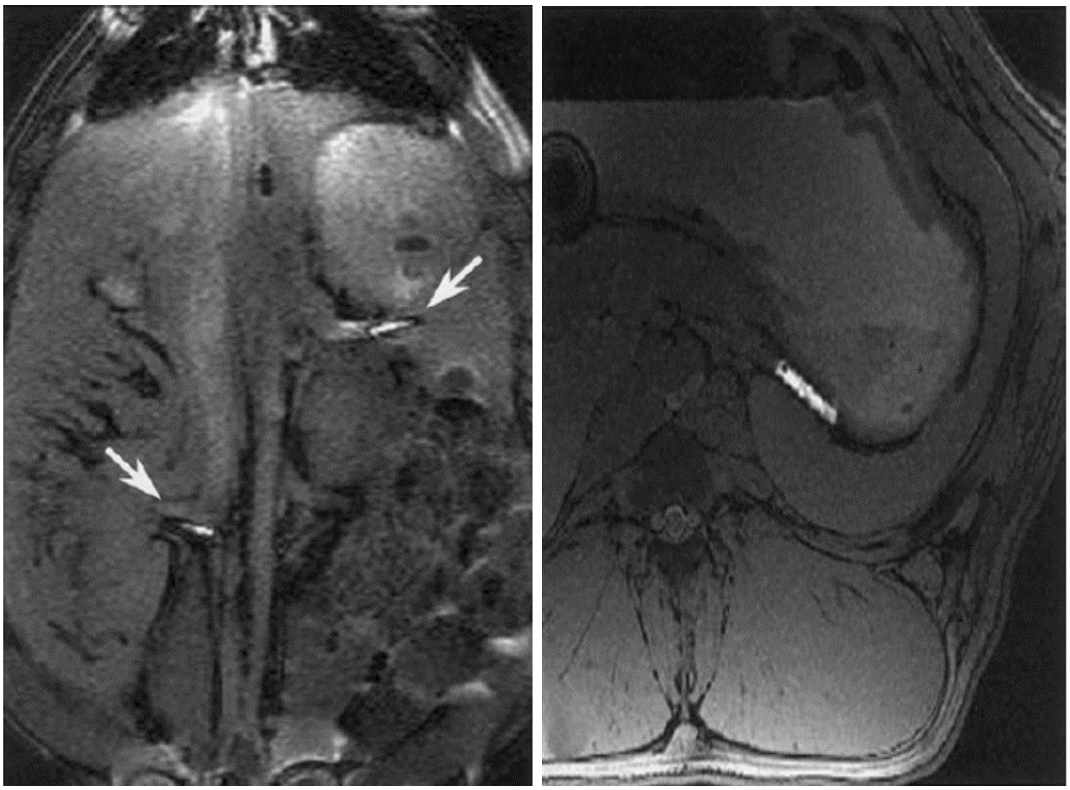

(a) The FISP localizer image showing stents (b) Image acquired during one breath-hold

Figure 2.1. In vivo images acquired with stents implanted into the right renal artery and the splenic artery of a pig [12].

Several methods have been developed to limit or minimize the active device heating, including detuning the devices during radio frequency transmission (two channels), the use of RF chokes [50] or transformers [51] in transmission lines to modify the elec-

trical length under MRI. However, although their promising improvements in terms of RF induced heating problem, none of these techniques can offer an active device design that can have clinically acceptable mechanical performance such as pushability, torqueability, flexibility, and kink resistance [39].

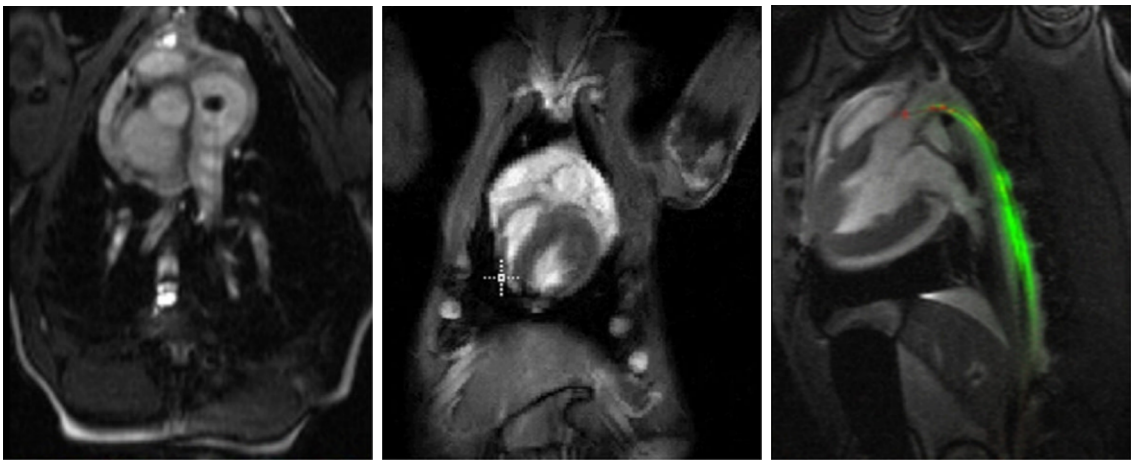

(a) Passive balloon catheter (b) Active tracking catheter (c) Active guidewire

Figure 2.2. Three representative approaches to catheters designed to be tracked using cardiovascular magnetic resonance (CMR) [19].

2.3. Coil Design for MR Detection

Regarding MRI applications, coils are generally evaluated using remarkable parameters like B_0 homogeneity [52], B_1 uniformity [53], RF power efficiency [54], and SNR of their sensitive volume [55, 56]. Numerous strategies over the years have been investigated to increase sensitivity of the MRI experiment. One of the oldest strategies is to introduce successively stronger magnetic fields, as the sensitivity depends on the magnetic field. This solution, unfortunately, couples highly sensitive MR studies to large, heavy and expensive hardware that can limit versatility and portability. Fortunately the sensitivity also depends on the magnitude of the radio frequency (RF) field per unit current, which has prompted parametric studies of both typical and atypical RF coil designs used in magnetic resonance. These studies have led to the development of so-called microcoils (typically, coils with outer diameters around 1 mm) for enhancing MR sensitivity [57].

The first microcoils were produced via hand winding solenoid coils with small gauge copper wire, though in recent years a number of alternate fabrication methods have been introduced, including lithographic production. For example, techniques for planar MR microcoil fabrication have been used extensively, drawing on fabrication techniques of microelectronic and micro mechanical devices, such as lithography, electroplating and moulding [58–62]. However, these coils typically have magnetic field inhomogeneity and susceptibility effects, and are not always optimally shaped to maximize the filling factor. The results are less than optimal signal to noise ratio (SNR) of the MR measurement [57].

The use of solenoids over other coil geometries is the typical approach for alleviating some of these problems and achieving optimal sensitivity. Recent methods have been reported for producing three dimensional shapes such as micro solenoids or even saddle coil forms, including focused ion beam sputtering [63,64], micro contact printing using elastomeric stamps [65,66], and 3D laser pantography [67].

2.3.1. Dipole Characteristics and Geometry of Helical Coils

Helical coils are simply conductive windings in helices around a core or in a medium. Depending on their dimensional parameters including separation between turns, having constant or changing diameter etc., the helical coils have different names. Straight helical coils are the most common types of helical windings, and has wide range of applications in antenna design due to their well-known characteristics. Tilted helical coils differ from the straight ones by having a constant or changing angle of winding.

As current moves through straight wires, it creates a circular magnetic field around them. This is explained in Ampere's Law, Equation 2.1. This is a general expression for straight wires, to state the magnetic flux density of a point having a certain distance from the wire. Introducing the curvature of helices, or coil windings, this formula needs an integration and rearrangement to show the magnetic flux density at a certain point in Cartesian coordinate system which has the central start point of helix as its origin. Biot-Savart's law predicts that the magnetic flux density at an

arbitrary point, $M(x, y, z)$, for a certain current path C with a constant current I, in Equation 2.2. The value of r depends on the geometrical representation of the helix. Therefore, the magnetic field of each helical coil can be obtained once its geometrical formula is known.

$$\oint B.dl = \mu_0 I \tag{2.1}$$

$$B(x, y, z) = \frac{\mu_0 I}{4\pi} \oint \frac{\vec{dl} \times \vec{r}}{r^2} \tag{2.2}$$

Iterative calculation of this integration for special helical coils, the magnetic flux density can be observed in Cartesian system. Straight helical coils creates a strong magnetic field through the longitudinal axis. The uniformity of magnetic field is low, but the directionality is strong in the main field path.

As helical coil creates magnetic field in space, it is also possible to create current within a coil by introducing a changing magnetic field around it. This phenomenon is known as Faraday's Law which is expressed in Equation 2.3.

$$\varepsilon = N \frac{(d\phi_B)}{dt} \tag{2.3}$$

In the Equation 2.3, ε is the electromotive force, N is the number of turns, ϕ_B is the magnetic flux through a single loop.

In MRI applications the existing RF magnetic field generates current within the coil structure, as coil's magnetic field directionality matches with the direction of the RF field. Therefore, straight helical coils can provide imaging on one plane, due to

their directionality which is on longitudinal axis. On the other hand, tilted helical coils creates and absorbs magnetic field on more than one planar surface. But the magnetic response of tilted helices is not the same in all surfaces. Although they can create magnetic fields at more than one Cartesian surface, their peak response occurs at their tilting axis. In order to solve this problem, and create a uniform magnetization a second tilted coil is winded around the first one with a minus tilting angle to form a tilted double helix.

2.3.2. Straight Helical Coils

Equations 2.4, 2.5 and 2.6 show the general mathematical expression of straight helices in Cartesian coordinate system. R is the radius of the curvature of the helix, h is the separation between turns, and θ is the angle in radians which defines the turn number when divided by 2π.

Using θ as the integration variable, the straight helix geometry was plotted in 3D, which can be seen in Figure 2.3. For this example plot r was 10 mm, h was 2 mm, and θ had a limit value of 20π, which resulted in 10 turns. When current flows through straight helical coils, it create a strong magnetic field perpendicular to the plane of curvature. The main direction of the magnetic field was on z-axis, having a 0^0 or 180^0 polarity depending on the direction of the current flow. Due to strong one axis magnetic field direction of straight helical coils, they result in highly visible catheter images on one axis under MRI. However, the images are almost lost on the other two directions which are perpendicular to axis of coil magnetic field. Therefore, for interventions with MRI, straight helical coils do not have the sufficient characteristics, although they have common use in applications.

$$x(\theta) = rcos(\theta) \tag{2.4}$$

$$y(\theta) = rsin(\theta) \tag{2.5}$$

$$z(\theta) = h\theta \tag{2.6}$$

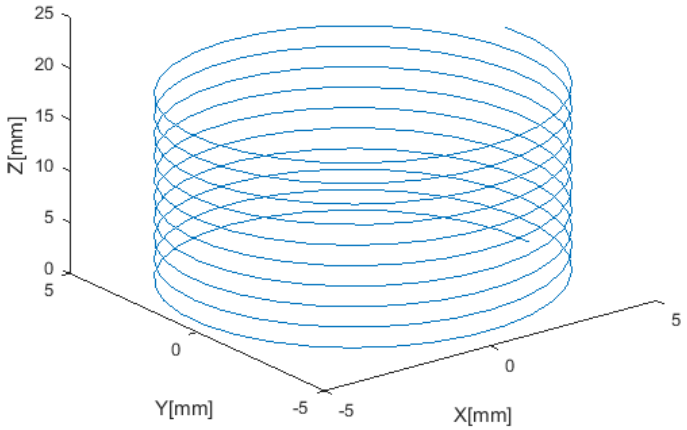

Figure 2.3. 3D representation of straight helix.

2.3.3. Tilted Helical Coils

The general mathematical representation of tilted helices differs from the representation of straight helices in only the derivation of z-axis component. The tilt angle is inserted into expression at this part by a multiplication of cotangent of tilt angle α, sinus value of θ and the radius of curvature, which is stated in the Equations 2.7, 2.8 and 2.9.

Same variable values were used for the 3D plot of tilted helix, in Figure 2.4. The extra variable – tilt angle- was defined as 38π /180 which is equal to 38^0. When current flows through tilted helical coils, the resulted magnetic field has the tilt angle with the longitudinal axis of helix in Cartesian system. For this plot the direction of the magnetic

field makes 38^0 or 218^0 with z-axis, which is determined by the direction of the current flow. Since the direction of the magnetic field has an angle with the fundamental axes of Cartesian system, it has components on more than one axis, which increases the chance of visibility in different directions under MRI. This magnetic field directionality of tilted helical coils, which has a projection on different planes, makes them a better candidate as catheter tips for MRI applications.

$$x(\theta) = rcos(\theta) \tag{2.7}$$

$$y(\theta) = rsin(\theta) \tag{2.8}$$

$$z(\theta) = \frac{h}{2\pi}\theta + rcot(\alpha)sin(\theta) \tag{2.9}$$

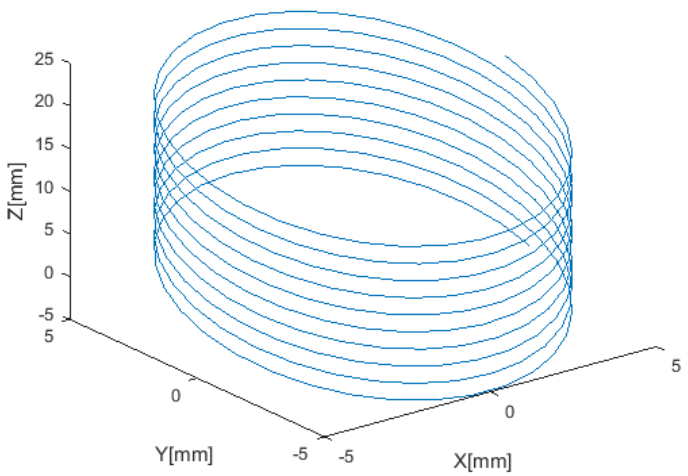

Figure 2.4. 3D representation of tilted helix.

2.3.4. Double Tilted Helical Coils

A double tilted helical coil is composed of two different tilted helical coils on top of each other having same of different parameter values. Equations 2.10 and 2.11 show the z-axis components of the tilted helices which forms a double tilted helix together.

Choosing h and θ values equal two tilted helices with similar characteristics will be formed. The values of radius of curvature r should differ from each other by the thickness of wire when a double tilted helical coil is formed. The value of tilt angle α should be selected in different signs to create symmetrical directions. Figure 2.5 has the image of a plotted double helix with the same h, θ, and r values of the previous helices, and α_1 was 380 and α_2 was -380.

$$z_1(\theta_1) = [h_1/2\pi]\theta_1 + r_1 cot(\alpha_1) sin(\theta_1) \tag{2.10}$$

$$z_2(\theta_2) = [h_2/2\pi]\theta_2 + r_2 cot(\alpha_2) sin(\theta_2) \tag{2.11}$$

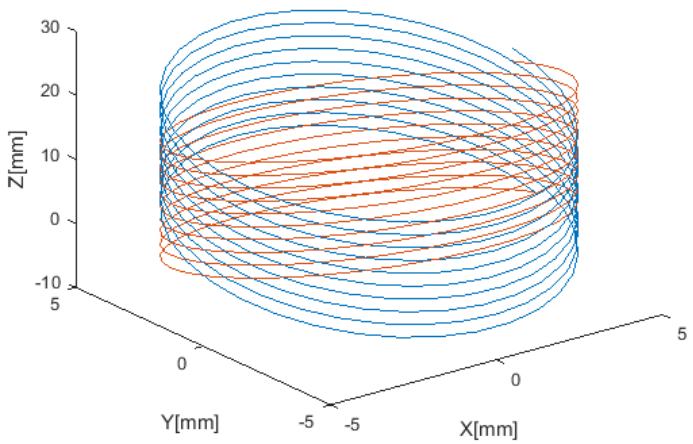

Figure 2.5. 3D representation of double tilted helix.

Considering the helices connected at the one end, and the current flows from the free and of the inner coil to the free and of the outer coil through this connected mutual end, B_1 and B_2 magnetic flux densities are generated by the coils, which can be seen in Figure 2.6. Each field has components on longitudinal and transverse fields which are B_y and B_z. Having all dimensional parameters the same the magnitude of those components are the same. However, their directions are different. B_z vectors cancel

each other and the combination of By components creates a strong transverse component. It is also possible to obtain longitudinal component for magnetic field by setting unequal tilting angles for coils, which prevents the components to cancel each other out. Strong transverse magnetic field of tilted double helical coils improves the visibility of catheters under MRI. Having the effects of each tilted coils into consideration, the resulted magnetic field can be calculated with the Equation 2.12.

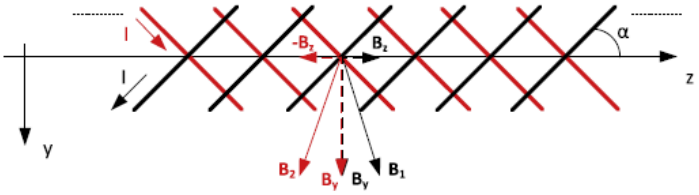

Figure 2.6. Magnetic flux densities of each helix in double tilted helix.

$$B(x,y,z) = \frac{(\mu_0 I)}{4\pi} \oint \frac{d\vec{l}_1 \times \vec{r_1}}{{r_1}^2} - \frac{(\mu_0 I)}{4\pi} \oint \frac{d\vec{l}_2 \times \vec{r_2}}{{r_2}^2} \tag{2.12}$$

3. DESIGN AND SIMULATION OF HELICAL COILS

3.1. Design

Computer simulation step of this thesis study started with creation of 3D models of the helical coil objects. FEM simulation programs needed CAD designs of the object to define and solve physics on the models. SolidWorks program was used to create solid helical coil objects depending on the mathematical modelling of structures. Either tilted or helical, each helix coil structure was modelled via this design program, and following that these models were transferred to the COMSOL Multiphysics program to solve the related physics.

The simulated coil models had to be matched with the fabricated objects, in order to provide a controlled study. Therefore, realistic objects were needed to be created for simulations. The dimensions of the copper wire, which was used in fabrication of coils, were measured for this purpose. Both the conducting copper layer and insulator layer surrounding it were measured under microscope. It was found that the copper thickness was 270 μm, and the insulator layer thickness was 30 μm. Figure 3.1 presents the photo of the copper wire taken under microscope.

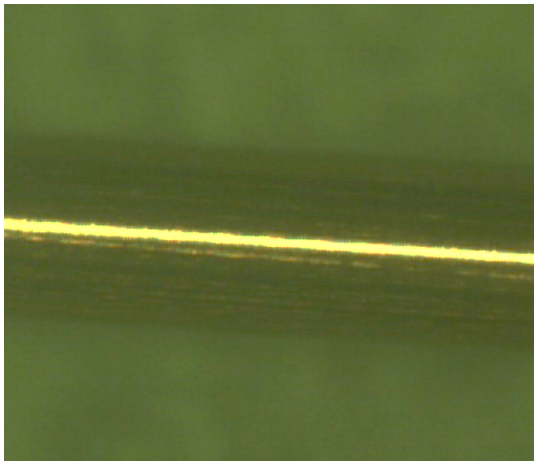

Figure 3.1. Thickness measurement of copper wire via microscope.

The design of each helical coil was started with modelling of the 3D curve by using the related equation of helix type. Radius of curvature, turn number, the separation between wirings, tilt angle and other parameters were defined on this curve. 2 lines of 20 mm, which would be wire extensions later on, were added to this helical curve. A plane was defined on the one end point of one of this line extensions, and a circle with the diameter of conductor – 270 μm - was drawn on it. By using the swept function of the design program, the integration of the circler area over the 3D curvature was achieved, and a solid helix structure was created by this. A core cylinder was extracted by another circle drawn on the front plane with the diameter of the 2 times radius of helix to form the plastic core which then be used as a template object to fabricate the coils. The same methodology of creating 3D helix then reused to create an insulator layer around it with the thickness of 30 μm. The winding, insulator layer and cylinder then assembled together to sketch the helical coil.

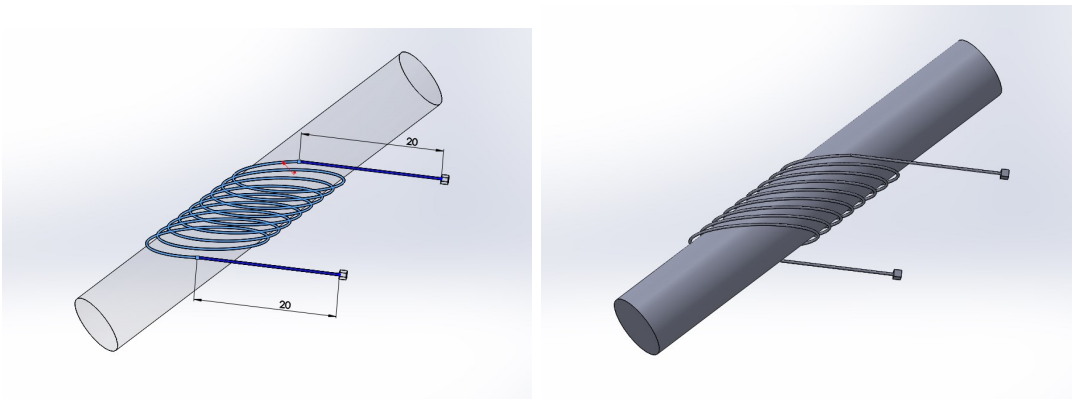

(a) Coil winding around plastic core (b) Assembled structure

Figure 3.2. 3D design of a coil.

The separation between the turns were defined as 2 mm for every model. This value was selected by considering the fabrication limitations of the available equipment. The trials for fabrication of template core objects having closer separation between the turns failed. Due to that, constant pitch was used for the studies. On the other hand 2 different diameter were chosen for both tilted and straight helical coil models. Objects with 10 mm and 5 mm diameters were designed with the CAD program. For each diameter and each helix type, the turn number was also kept as a variable. 2.5, 3.5,

4.5, 6.5, 8.5, 9.5 and 10 turn coils were designed with changing diameters and types. The reason of creating objects with decimals is the ease of assembling conductor and insulator layers in the SolidWorks program due to the asymmetry that they create.

The only difference of designing tilted and straight helical coils is the mathematical change in the z-axis representation of two structures which was defined in Chapter 2. Other than that, design steps are identical, because of the dimensional parameter equality.

3.2. FEM Simulations

In order to conduct the simulations as realistic as possible, the matching 3D models with fabricated helical coils were imported by the simulation program after completing the CAD designs. Domains and boundaries such as coil surface, core, wire, surrounding media were defined, and additional objects were added to the models at necessary steps. The materials were assigned to each part. Copper was used for the wire domain, and polyethylene was assigned to insulator layer. The material for core was selected as acrylic plastic, and surrounding domain was chosen as air. Material definition step was followed by mesh creation. Tetrahedral structures with changing dimensions were defined for every part of the model to solve the physics laws for radio frequency waves and magnetic fields. Figure 3.3 shows the meshed structure having helical coil, core, surrounding domain and infinite elements domain.

3 different studies were applied to helical coils during simulations to solve the dependent physics. The first one included the magnetic field study of AC/DC module of COMSOL Multiphysics program for stationary conditions and frequency domain. This operation resulted in computation of inductance value of coils as well as magnetic field magnitude and directivity with changing frequency. The second study covered the Electromagnetic waves physics of Radio Frequency module. Eigenvalue equations were iteratively solved to acquire the resonance frequency of structures. Another study used the same physics of Radio Frequency module, but this time for frequency domain to derive the frequency response of the designs.

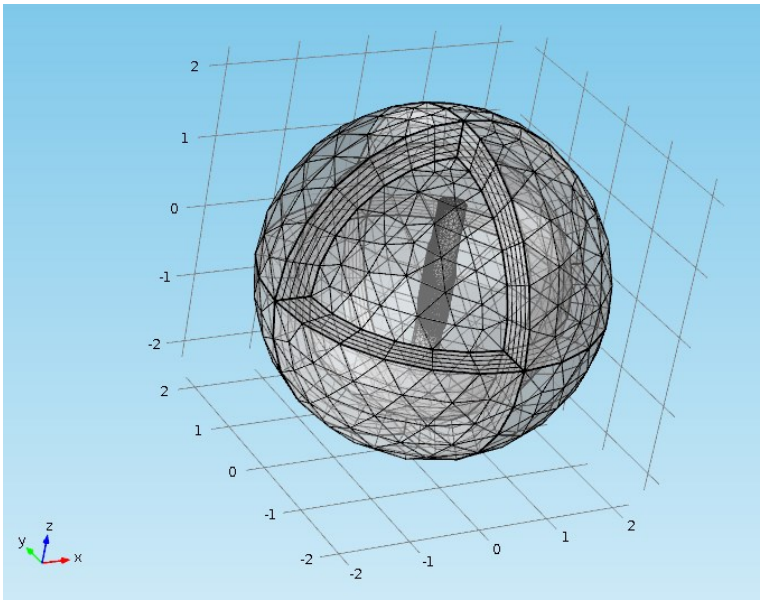

Figure 3.3. Meshed coil structure in the simulation model.

3.2.1. 3D Design Transfer and Mesh Creation

The CAD model files generated by SolidWorks program were imported to the created geometry in FEM simulator program. In addition to this imported helix coil structure, a sphere with an approximately 10 times larger dimension than core cylinder defined around the helix for infinite element domain and perfectly matched layer definitions depending on the physics. Domain and boundary definitions were achieved for easy material assignments and physics definitions. Following that relevant materials were defined for each domain and special boundary.

Mesh creation implemented after that point. Starting from the elements with smallest dimensional parts, meshes were built through the outer dimensions of the complete structure. Especially conductor and insulator layers, and the close domains to these parts were meshed extremely fine to be able to run the simulations without errors. Due to the wiring of a thin cable around a relatively large cylinder, the number of meshes in wire domain was higher compared to the other domains. A closer look to mesh around tilted helix structure can be seen in Figure 3.4.

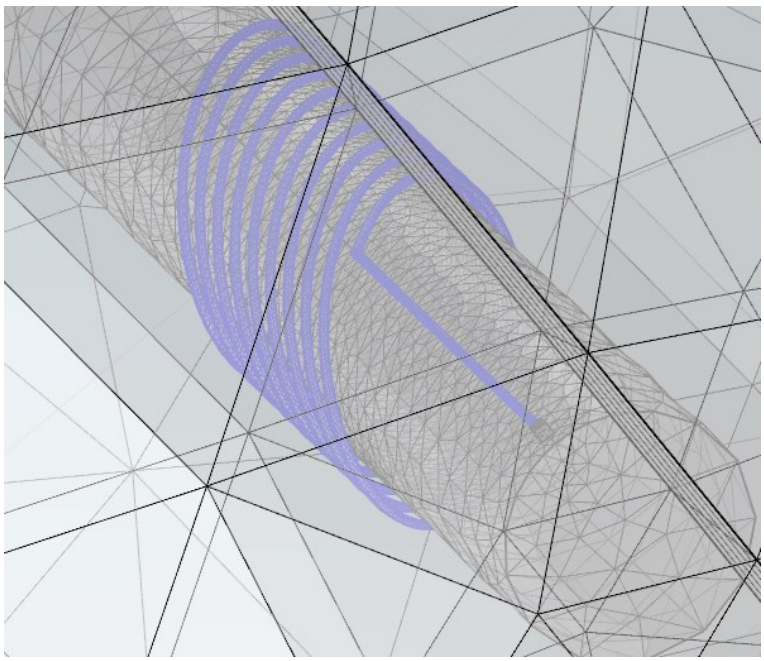

Figure 3.4. Closer image of created meshes for winding and plastic core.

Two approaches were followed to achieve meshing of design without intersecting boundaries or errors. In the first approach, a fine mesh was created only for the end surface of the windings and insulator around it. This surface mesh then was swept through the wire and insulator domain similar to the creation of helix model, and additional triangles were defined in between swept units to build triangles in the domain. The same method was repeated for cylinder, and larger meshes were generated for remaining air and Perfectly Matched Layer (PML) domains. Meshes were built fine with this method. However, the simulations failed after a certain point although there were no error in the mesh generation step. Second approach include extraction of larger domains such as air and PML, and letting the program to generate variable length meshes depending on solved physics for smaller components, such as conducting wire and thin insulator layer around it. After that point, meshes were created manually for larger domains. Enabling this method for creating meshes resulted in successful simulations.

3.2.2. Magnetic Field Studies

The aim in carrying out the simulations is finding the inductance value, resonance frequency and magnetic responses of the tilted and straight helical coils. Those required parameters depends on magnetic characteristics. Therefore, magnetic field studies of AC/DC module which is presented in COMSOL Multiphysics Program were applied to the geometries. Stationary, and frequency domain simulations were actualized, and the outcomes were noted. The magnetic fields studies includes Ampere's Law, magnetic insulation definitions, and impedance boundary conditions as default physics. Additional physics definitions took place regarding the requirements of the study. The outer spherical surface was defined as the Infinite Elements Domain (IED) to achieve the physical computations.

3.2.2.1. Inductance Calculations. On account of calculating the inductance, Single Turn Coil (STC) definition was added to preset physics with a boundary feed and ground port. Those ports were defined by removing small parts from each two ends of the winding domain out of the effective domain list of magnetic fields, and setting up the ports to the two end surfaces.

Stationary simulation were carried out at this point to get the initial results. The computations were achieved successfully. Once the simulation of the study was ended, a data set for solved physics and default plot of magnetic flux density were provided automatically. Calculating the inductance were achieved by solving magnetic power dependency of inductance, which is stated in the Equation 3.1, for the available data set.

$$U_m = \frac{1}{2} L I^2 \tag{3.1}$$

The plot in Figure 3.5 includes the data points which are the results of the simulations of 10 mm diameter tilted helical coils with 2 mm pitch having changing turn numbers. 6 different designs were simulated, and their inductance values were derived. It is clear that there is a linear relation in between number of turns and inductance value. This dependency were drawn by using linear interpolation approach.

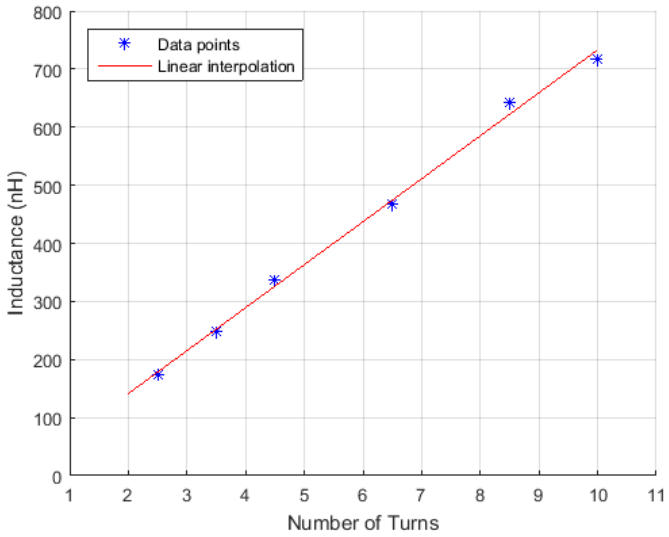

Figure 3.5. Simulated inductance values of tilted helical coils with 10 mm diameter.

This simulations and inductance derivations were repeated for all designed model files. 26 helical coils with equal tilted and straight helixes were defined in program and their FEM simulations were implemented. The complete results of those simulations are available in Figure 3.6. For both tilted and straight helices, the linear dependency in between number of turns and inductance value is valid. The main difference is tilted helical coils shows a steeper linear dependency when compared to the straight helices with same diameter and turn numbers. That is an expected effect of tilted helices since the total conductor length contributing to the magnetic field is larger in tilted helices although the surrounded cylinder has the same dimensions. This additional contribution of copper wire to magnetic field increases the total magnetic power around the coil, and results in higher inductance values. This fact can be simplified as comparing the magnetic fields of a circle and an ellipse which have same vertical dimensions.

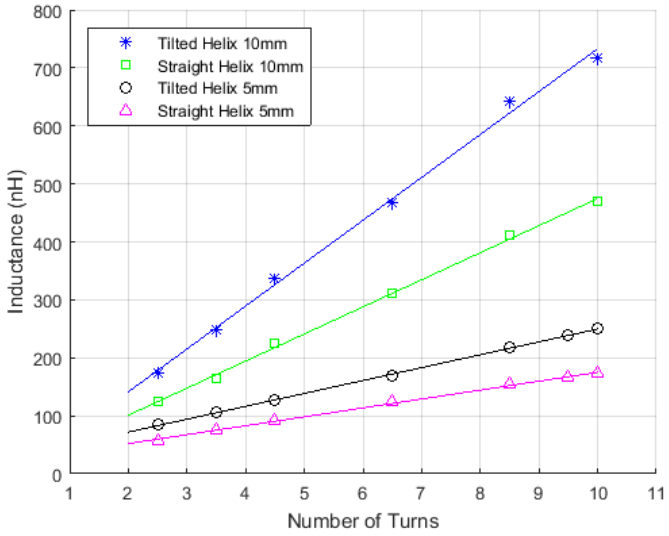

Figure 3.6. Inductance values of all simulated helical coils.

Diameter change also resulted in similar effects for both tilted and helical coils. As the diameter increases the inductance increases in parallel. Coils having equal pitch, equal turn number but larger diameter have higher inductance values. Another effect of diameter change is, helical coils with larger radius of curvature has an improved linear dependency of number of turns on inductance. The plot of complete measurements indicates those characteristics.

3.2.2.2. Magnetic Fields and Frequency Response. Magnetic fields were solved for helical coils by disabling boundary feed and ground surfaces, and introducing the lumped port. Same edges used for lumped port definition. Coaxial cable were defined outside of wire domain starting from these edges, matched to 50 Ω standard value. Current excitation was enabled from this port to compute the results of the equations. Following necessary changes, the structure was simulated from 1 GHz to 1.8 GHz with 100 MHz step size. The frequency dependent simulations takes longer time, because of the repeat of each successful computation, which is a result of extensive iterations, for every step in the desired frequency range. It is a combination of the solutions for each single frequency point.

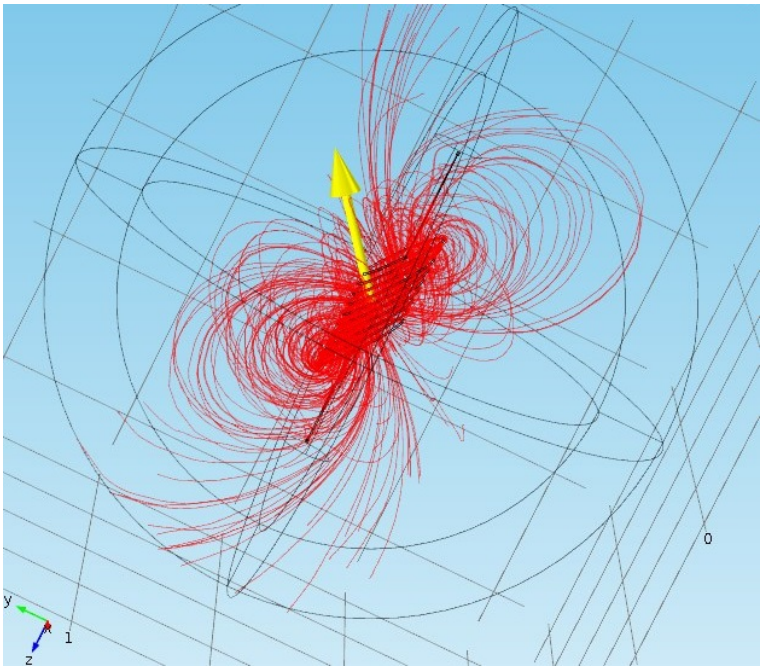

Figure 3.7. Magnetic flux density stream lines for tilted helical coil.

The plots for magnetic flux density and magnetic field norm were generated as default, once the simulations were completed successfully. Plane cuts were defined on 3D, and magnetic field of the geometry intersecting with those planes were visualized. In addition to x, y and z planes, the plane which had tilt axis as normal vector was also defined. In Figure 3.7, the 3 dimensional magnetic flux density streamlines were plotted for 8.5 turn helical coil with 10 mm diameter. The streamlines shows the magnetic flux density contours. The arrow shows the direction of B in 3D, and this direction is almost identical with the tilting axis.

In Figure 3.8, the magnetic field norm was observed for the same helical coil at its resonance frequency, which was 1.3 GHz. The magnetic field is intense around the windings of the tilted helical coil both out of the coil and within the core object. The magnetic field diminishes rapidly as the distance to coil surface increases. The value of the magnetic field norm drops down to 1E-11 range near infinite elements domain, which was on the range of 1E-3 for closer points to the windings.

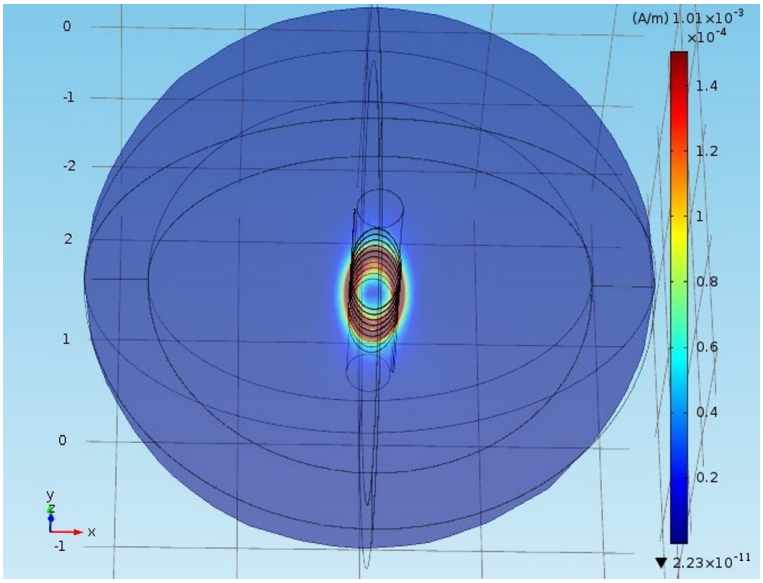

Figure 3.8. Magnetic field norm plot of tilted helical coil.

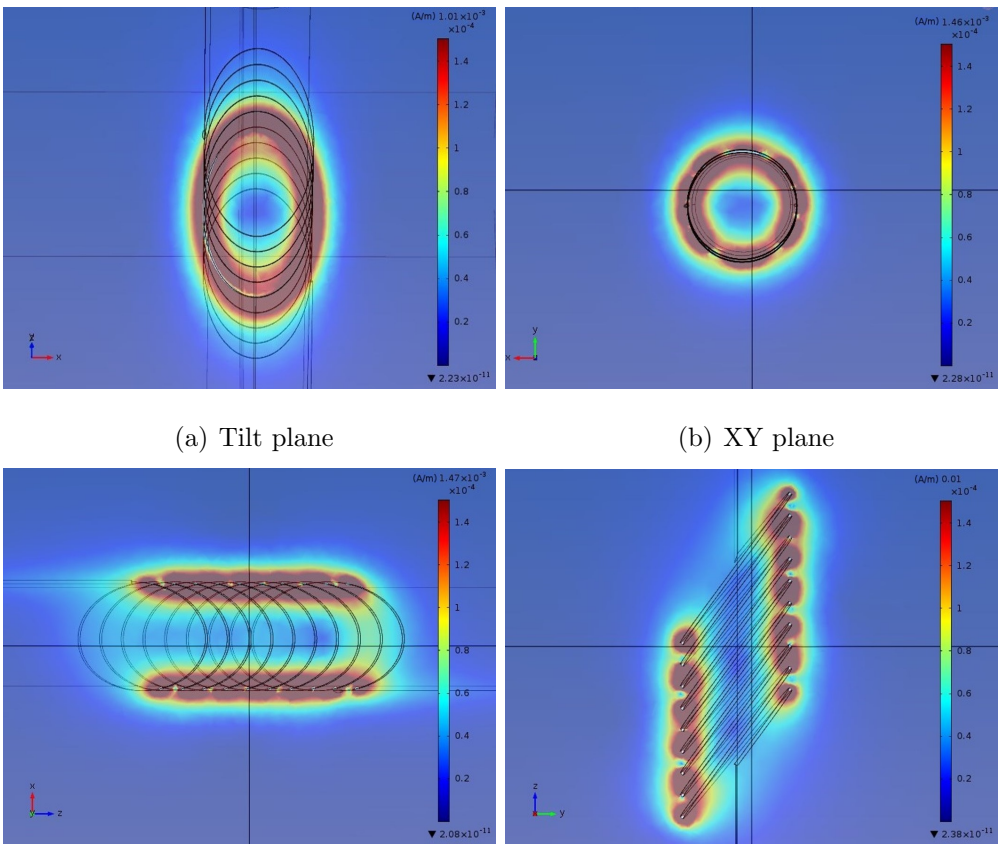

(a) Tilt plane

(b) XY plane

(c) XZ plane

(d) YZ plane

Figure 3.9. Plane dependent magnetic field norm plots tilted helical coil.

Figure 3.9 has four images which were taken from the x,y,z and tilting surface cuts of magnetic field norm for the resonance frequency of tilted helix of 8.5 turn with 10 mm diameter. From these images, it can be concluded that the magnetic field is denser for tilted helical coils on their tilting surface. As plane of visualisation changes, the reduction in the magnitude of magnetic field can be noticed. The thickness of the region that has strong magnetic field changes as the intersecting plots surface changes. This thickness indicates the magnitude of the magnetic field norm on that specific surface. On tilting surface, the magnetic field norm is maximized for tilted helical coils. On general axes - XY, XZ and YZ planes - magnetic field effective region thickness reduces. However, there is still magnetic field component thanks to the angler variation of the structure. On straight helical coils, magnetic field is strong in XY plane. However, it almost drops down to zero on other planar surfaces. This is because of the magnetic field directionality of the straight helical coils, which has only one general axial component.

As the plots of magnetic field norm generated for changing frequencies, the effects of resonance were also monitored. In Figure 3.10, the images of magnetic field norms for 1.2 GHz, 1.3 GHz, 1.5 GHz and 1.8 GHz were plotted. At resonance frequency, the field norm peaks in magnitude. The field within and around the coil increases tremendously at this specific frequency. As the frequency moves up or down from the resonance frequency the field drops significantly, and this fact can be seen in the related images. For every step frequency in sweep calculations, the magnetic field norm was plotted. The effect of resonance is noticed clearly when the fields on plots are compared. However, this was a manual search method, and it is easier to capture the resonance frequency with the help of parameter plots, such as S_{11} and lumped port impedance.

Using the frequency sweep simulations for magnetic field studies the port impedance calculations were achieved for every step frequency. Plotting this data together, the change of impedance as frequency shifted was monitored. This change directly states the resonance frequency. Figure 3.11 shows the lumped port impedance versus frequency. At resonance the port impedance makes a sharp peak. This plot indicated that the resonance frequency was at 1.32 GHz, and this is very close to the manually

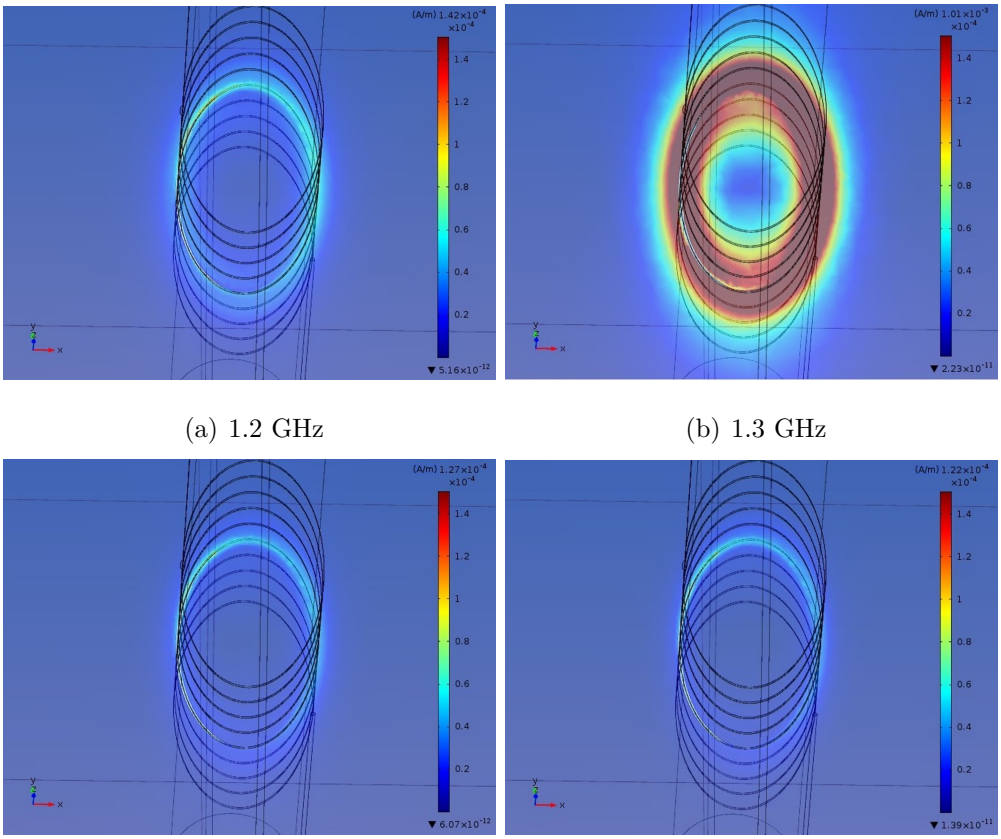

(a) 1.2 GHz (b) 1.3 GHz

(c) 1.5 GHz (d) 1.8 GHz

Figure 3.10. Frequency dependent magnetic field norm plots tilted helical coil.

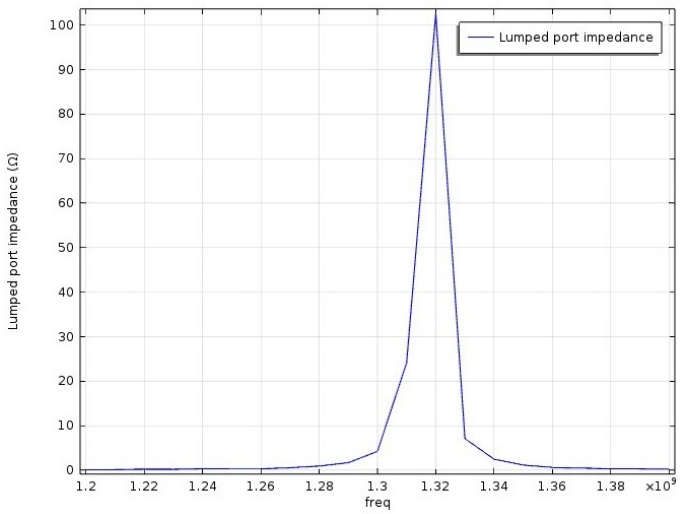

Figure 3.11. Lumped port impedance change with frequency for 8.5 turn tilted helical coil with 10 mm diameter.

extracted value of surface plot search which was noted as 1.3 GHz. The frequency range in the plot was narrowed, to visualize the peak at the resonance frequency clearly.

3.2.3. Resonance Frequency Derivation

One other study were run during simulations to calculate the resonance frequency directly without observing the plots or searching the effects of resonance. Electromagnetic waves studies were enabled for helix design under Radio Frequency module. This module and related studies are set to design antennas, wave-guides, filters, circuits, cavities and meta-materials. Electromagnetic wave propagation and resonant behaviour are simulated via this RF module to compute electromagnetic field distributions, transmissions, reflection, impedance, Q-factors, S-parameters, and power dissipation. Multiple physical effects can be coupled together and consequently affect all included physics during the simulation of an electromagnetic device or structure. For this study, eigenvalue solutions were generated to calculate the resonance frequency of device directly.

It is possible that the electromagnetic devices may have multiple resonance frequencies at different points. Especially at higher frequencies may introduce additional resonance effects for structures. It is possible to set the desired number of eigenvalues, and the related frequencies around which the eigenvalue solutions should be searched for. Defining these parameters will introduce initial values for the equations, and reduce the total time used for computing the solutions. For our case only one eigenvalue was set as desired number of eigenvalues, and the frequency to search the resonance around was typed as 1 GHz. Before running computations, again a lumped port was defined for the structure under this added RF physics branch. The end surfaces of wire was set for lumped port. The computation spent lower time than frequency domain study of magnetic field simulations. The result was 1.312 GHz for the same model which was the tilted helical coil with 8.5 turns and 10 mm diameter, which is almost identical with the solution found by searching the plots of magnetic fields frequency response. This eigenvalue computation is a fast and direct way to find the resonance frequency for structures.

3.2.4. Electromagnetic Waves – Frequency Response

Another frequency domain study was defined this time for electromagnetic waves physics to be able to realize the frequency shift effects of helical coil structures. RF module was reused for this analysis. Far field domain, impedance boundary conditions, perfect electric conductor and wave equations were arranged separately for domains and boundaries. The frequency sweep was set from 1 GHz to 1.8 GHz with a step size of 50 MHz. This simulation took the longest duration to finalize the computations. Increasing the step size, or reducing the frequency range decreases this duration. However, in order to distinguish the effects of resonance or frequency change explicitly, at least a certain range should be set as sweep range.

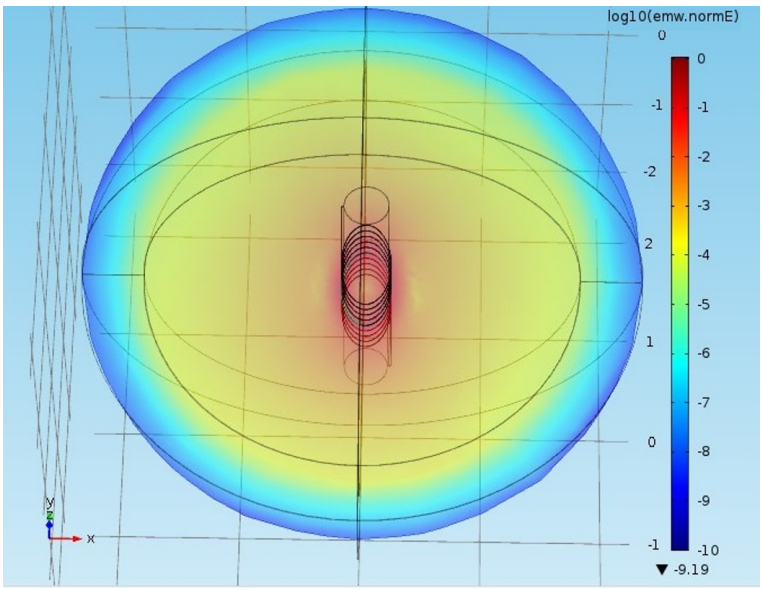

Figure 3.12. Electric field plot of 8.5 turn tilted helical coil with 10 mm diameter.

The solutions generated with this study were extensive. Multiple plots were generated for various frequencies including electric field norm, far field norm, S-parameters. The resonance characteristics were observed in all type of graphical representations and plots. Figure 3.12 shows the logarithmic scale of electric field E norm near resonance frequency for 8.5 turn 10 mm tilted coil. As it was expected, the field is strong near coil and diminishes through the boundary of surrounding field.

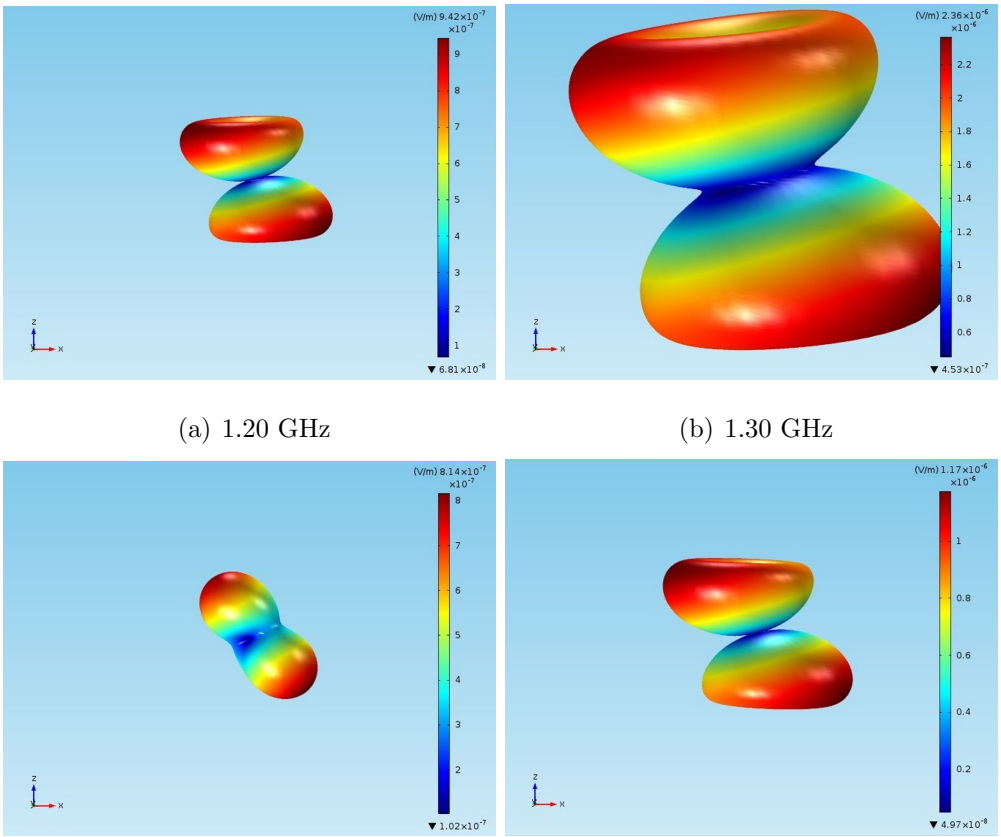

(a) 1.20 GHz (b) 1.30 GHz

(c) 1.35 GHz (d) 1.50 GHz

Figure 3.13. Far field plot of 8.5 turn tilted helical coil with 10 mm diameter.

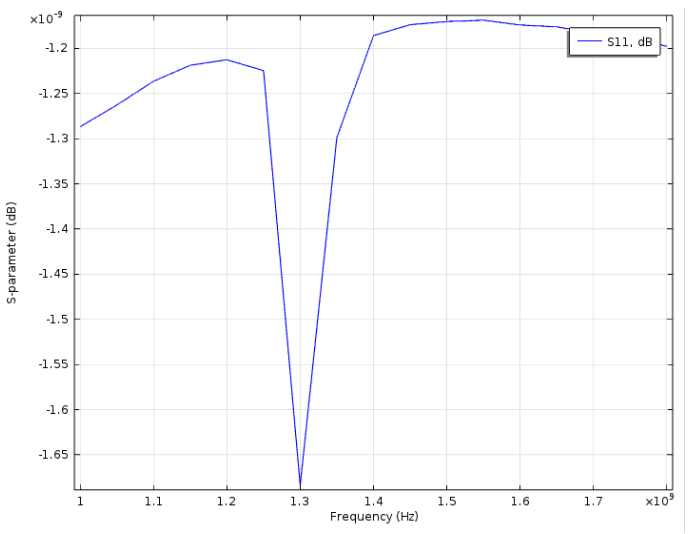

Figure 3.14. The plot of S_{11} for 8.5 turn tilted helical coil with 10 mm diameter.

In Figure 3.13, far field pattern of the same tilted coil was generated for its resonance frequency. Before computations, the far field was defined for surrounding domains of coil structure. The angler shift due to tilting of the coil can be visualized in this pattern. The change of far field were stated out with the help of the images of far field for changing frequencies. The frequencies of images are 1.20 GHz, 1.30 GHz, 1.35 GHz and 1.50 GHz respectively. The far field region maximizes with resonance, and just after resonance it reaches its minimum having radical changes in the pattern. As frequency continues to increase, the region becomes larger again. However, the peak point is reached at resonance frequency.

Figure 3.14 shows the magnitude response of S_{11} parameter generated with the results of this study. Around 1.3 GHz, the negative peaking occurred, which was the characteristic of resonance. Before and after this frequency reduced magnitude of S_{11} observed. The reason of the fall in the S_{11} is that at the resonance frequency the signal is transmitted from the coil. Therefore, a decrease in the reflected signal is observed. Since this parameter is also called as reflection coefficient, the reflection decreases at the resonance frequency.

4. FABRICATIONS AND MEASUREMENTS

It was necessary to fabricate the tilted and straight helical coils, for which the FEM simulations are conducted, in order to state out the reliability of the simulation processes. For this purpose both coil structures are fabricated to form related inductor structures with the same macro scale that is used in the simulations. Before the simulation steps the thickness of the copper layer and the insulator layer of the wire was measured via microscope to provide dimensions for the computer based 3-dimensional designs. Same wire is used to create tilted and the straight helical inductors for this fabrication step.

In order to bring out the fabricated helices four different plastic cores were designed and 3D printed. This template provided a solid object to perform windings around it without much differentiation with the computer designs. Helices are created for both tilted and straight structures with changing diameter, turn number and length, which was also the case for the FEM simulations. Characteristics of the 26 fabricated helices were measured via Network Analyzer with a specific probe design which was also created for this specific purpose. The electrical characteristics were measured as well as magnetic directionality of the objects in 3D. The results are discussed to state out the performance differences of the helices with respect to parametrical changes in design, and to show the reliability of the FEM simulations.

4.1. Inductor Fabrication

4.1.1. Design and Fabrication of Template Plastic Core

Reproducibility of the coil fabrications are very fundamental to prove that the followed methodology is reliable. In order to create identical helical structures, which were the subjects of the FEM simulations, and repeat this fabrication steps for every time that is needed template core objects are needed to perform windings around them. Initial attempts to create helical windings without a template objects failed.

Almost none of the helices were recreated, and it was not possible to control the design parameters such as pitch, winding diameter, length and tilt angle. Therefore, those attempts proved the requirement for the template core objects.

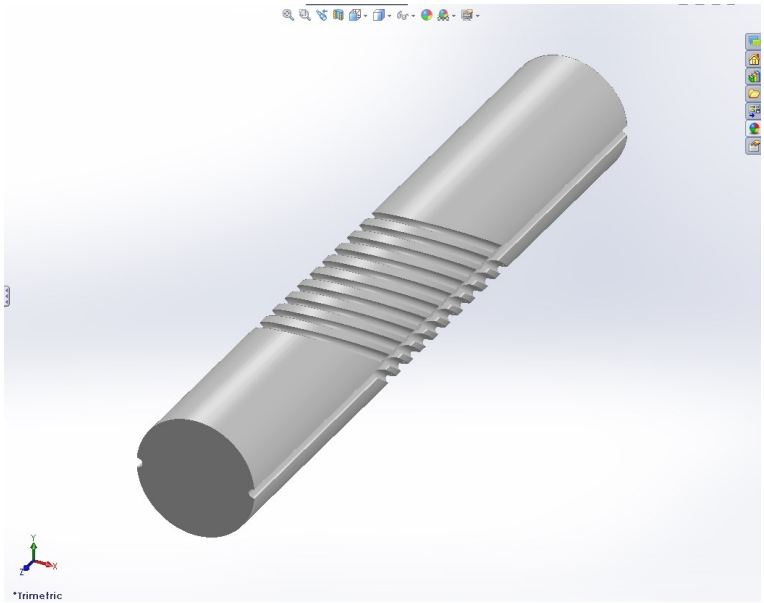

Figure 4.1. 3D design of template plastic core for tilted helices.

The design of the template objects are performed in SolidWorks. The mathematical equations to create tilted and straight helices in Chapter 2 were used to form helical cavities around a solid cylinder with the related dimensions. Taking the resolution of 3D printer which was available at the laboratory to create helices and the deviation in the dimensions due to plastic melting process in 3D fabrication, the cavities were designed slightly larger than the actual wire dimensions.

Four different plastic template core objects were 3D designed in computer, and 3D printed via Makerbot Replicator 2. The length of these objects are the same which is the sum of the length of 10 turn helix with 2 mm pitch and 20 mm straight wire extinctions, which makes 60 mm in total. Additional longitudinal cavities are created both sides in order to fabricate coils having turns with half numbers such as 4.5 and 8.5. The cavity dimensions were optimized after several 3D fabrications with different sizes and coil winding trials. 26 template core objects were created as final to bring out all helices which were simulated, excluding the objects used for test purposes.

4.1.2. Fabrication of Tilted and Straight Helical Coils

Copper wire having conductor thickness of 270 μm and insulating layer thickness of 30 μm is used to create helical coils. The copper wire is wrapped around the template core objects having diameter of 10 mm and 5 mm respectively. With the help of the designed cavities in the plastic template objects, the helical structure forms were preserved during the wrapping process of the wire. 26 helical coils were fabricated; 13 of them were tilted coils with tilting angle of 38^2, and 13 of them were straight helices. 6 out of these 13 pairs had a diameter of 10 mm, and the rest 7 had the diameter of 5 mm.

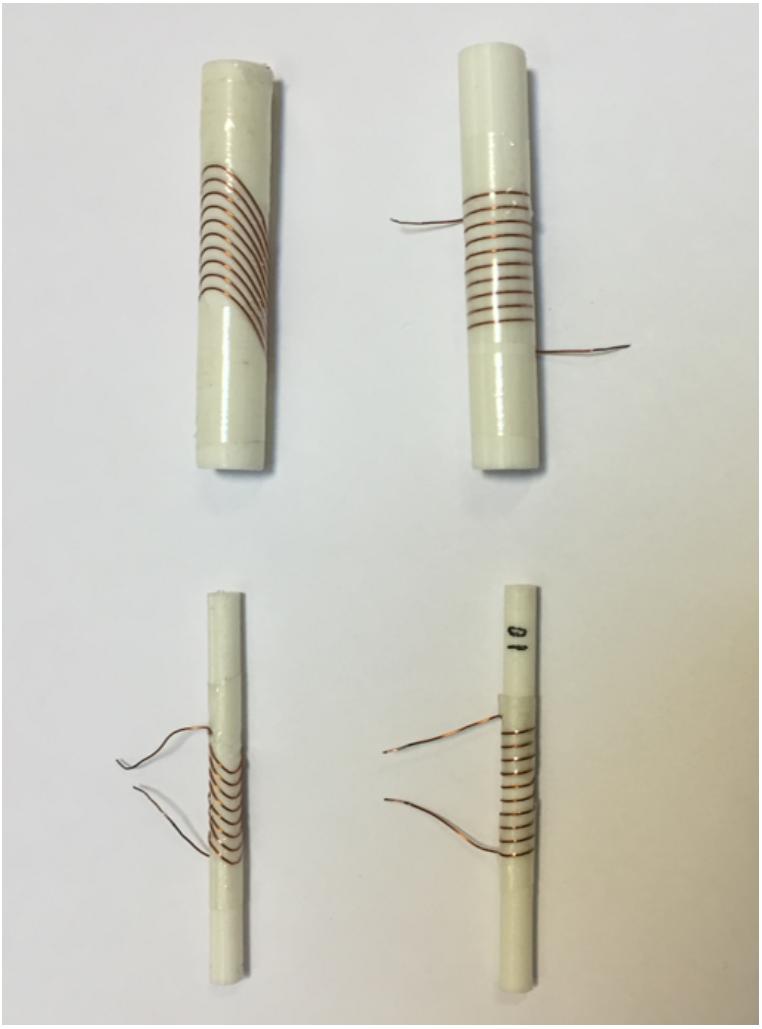

Figure 4.2. Fabricated coils with models.

In order to create direct contacts with the copper layer, the insulator layer around the wire had to be removed. This was achieved by burning and scraping off the insulator layer closer to the end points of the helix structures. The contact formation after removal off insulator layer was tested by multimeter. This process was repeated for all fabricated helix samples.

In addition to cavities which are formed around the plastic core, adhesive tapes were used locally for helices to make the structure steady. Especially for helices with lower turn numbers, cavities were not enough to hold the formation together.

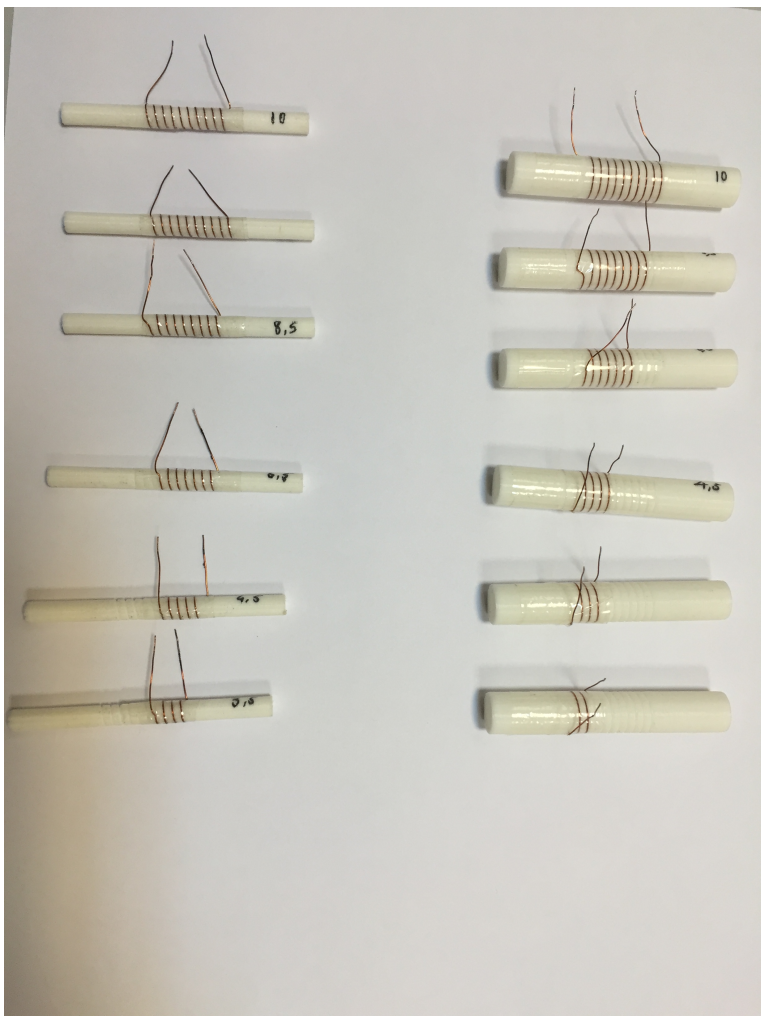

Figure 4.3. Fabricated straight helical coils of 5 mm and 10 mm diameters with changing turn numbers.

4.2. Measurement Setup and Calibration

The inductor characteristics, and magnetic directionality of the coils were tested using a Vector Network Analyzer. This measuring device is able to work within the frequency band of 300 kHz to 4 GHz, which is sufficient to perform the characteristics analysis of the created helical objects. One port measurement was performed during this laboratory study. Calibrations made manually for the specifically designed probes. Once the calibrations were done, non-contact search probe was used to make the measurement. The characteristics were observed for each helical coils. Further analysis on results were performed by generating special plots on MATLAB.

4.2.1. Calibration of Network Analyzer

In order to investigate the physical and electrical characteristics of the coils successfully, one port measurement were carried out using the vector network analyzer. At the beginning of the each study, the port has to be calibrated by using special probes. For this purpose 3 different calibration probes were prepared using coaxial cable, and electrical components. One end of each of 3 coaxial cable parts with a length of 20 cm were bound to SMA connectors. The other end of the first of them was left unconnected to create and open circuit calibration probe. The inner conductor and outer conductor layer parts of the second coaxial cable were soldered together at its respective end to create a short circuit calibration probe. A 50 Ω surface mount resistor with 0805 package were soldered between the conducting layers of the third probe to prepare the third and last calibration probe, which is the match probe.

These 3 calibration probes with the same length were used according to the one port calibration program of the vector network analyzer to calibrate the device. Once the calibration was done, Smith Chart generated by the device was used to test the calibration of the device, before moving forward to inductor measurements. When open probe was connected, the marker on the plot is on the right of the Smith Chart, which is the typical characteristics of the open circuits. Connecting the short probe moved the marker to 0 point, and connecting a 50 Ω resistor resulted the marker to appear

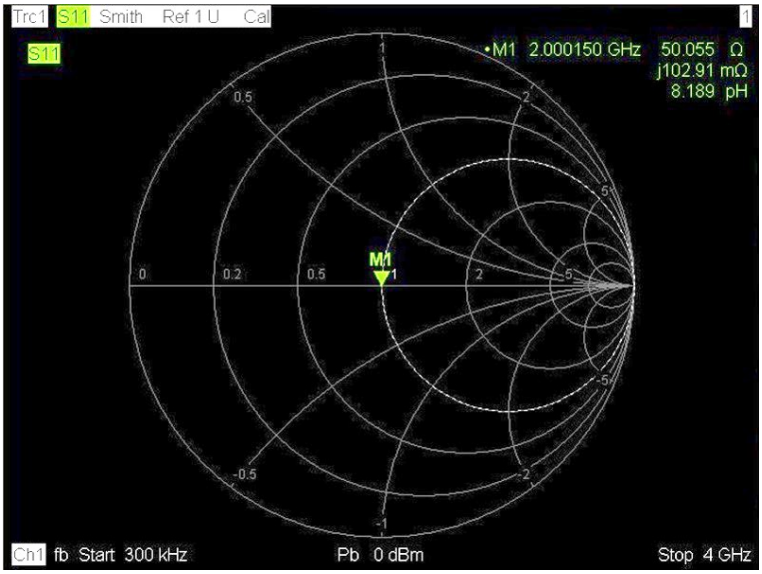

Figure 4.4. Smith chart caption of 50 Ω resistor measurement.

at the center. Connecting other electrical elements to probes resulted in expected characteristics. Figure 4.4 shows the measurement of 50 Ω resistor using these probes.

4.2.2. Inductance Measurement Method

The probe preparation were successful. However, connecting fabricated inductors as well as standard ones resulted in unexpected behaviours such as parasitics, and by using this method it was not possible to study the magnetic directionality characteristics of the inductors. Therefore, a new approach was needed to perform the measurements properly.

At this point, it was clear that the fundamental idea behind the catheter receiver tip design could work to achieve the inductor measurements; creating an LC circuit by connecting a standard capacitor, and obtaining its resonance frequency by observing the change in the reflection coefficient of a high magnetic field generating loop. The magnetic field generated by the larger coil will excite the LC structure significantly at its resonance frequency. By changing the frequency applied to large circular coil of the probe, and monitoring the frequency response of the S_{11} parameter the resonance

frequency of the LC structure can be obtained. Having the resonance frequency determined, the inductance can be extracted mathematically with Equation 4.1, since the capacitor value is already known.

$$L = \frac{1}{C(2\pi f)^2} \tag{4.1}$$

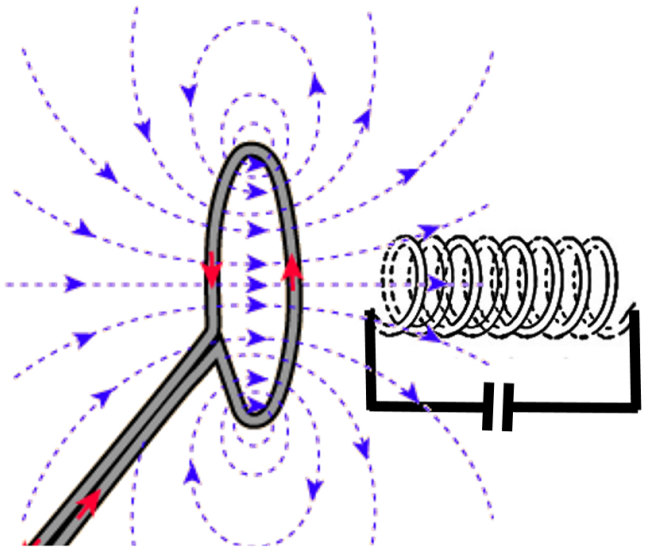

Figure 4.5. Excitation of the test inductor in the LC circuit by the magnetic field generated by the measurement coil.

4.2.2.1. Design and Fabrication of Non-Contact Search Probe. Non-contact search probe was used to generate magnetic field to induce current around the inductor of the LC circuits. And reflection coefficient of this probe was observed during the test studies to detect the resonance frequency of the LC circuits, at which the magnetic field excites the fabricated inductor. An SMA connector was assembled to 20 cm long coaxial cable, and a large circular inductor was soldered to other end which was generated by 3 loops turn of a thick copper wire. The area of this probe was large enough to allow the helical coils to move in and out easily to observe the excitation effects. The coaxial cable

length was chosen as 20 cm, that way the non contact search probe had the identical cable length with the open-contact, short-contact and matching calibration probes of network analyzer.

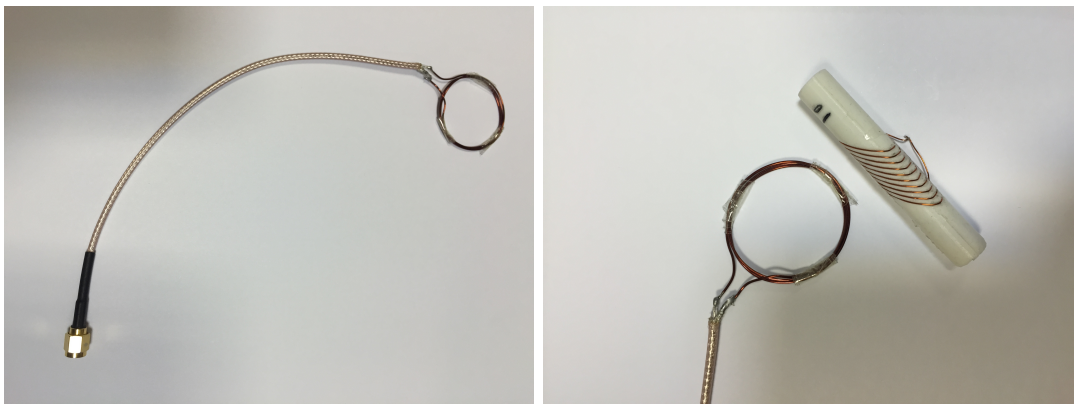

(a) Non-contact search probe (b) Probe and fabricated coil sample

Figure 4.6. Measurement preparations.

After fabricating the non-contact search probe, 3 LC circuits were prepared with a standard 820 pF capacitance and standard inductances. Inductances with values of 1 μH, 3 μH and 10 μH soldered to 820 pF capacitance to measure the resonance frequencies of their related LC structures. The resonance frequency of the LC structures turned out to be 5.57 MHz, 3.20 MHz and 1.76 MHz respectively, which are almost identical with the calculated values. These results proved that the non-contact search probe and inductance measurement method are reliable for the measurements of the characteristics of inductors. Table 4.1 shows this initial measurement test results.

Table 4.1. Test Measurement Results.

Inductor	**Capacitor**	**Measured Resonance**	**Extracted Inductance**
1.00 μH	820 pF	5.57 MHz	1.00 μH
3.00 μH	820 pF	3.20 MHz	3.00 μH
10.00 μH	820 pF	1.76 MHz	10.00 μH

4.3. Measurements of Tilted and Straight Helical Coils

Fabricated inductor values were measured by building LC resonator structures with a standard capacitance of 820 pF. Due to the excess resonator excitation, the change in the return loss of the non-conducting search probe stated the resonance frequencies. An additional calculation step performed to extract the inductance value. In addition to pointing out the inductance values, dependency of quality factor to design parameters such as number of turns, coil diameter were observed qualitatively. Directivity characteristics of tilted and straight helical coils were also investigated during this measurements step.

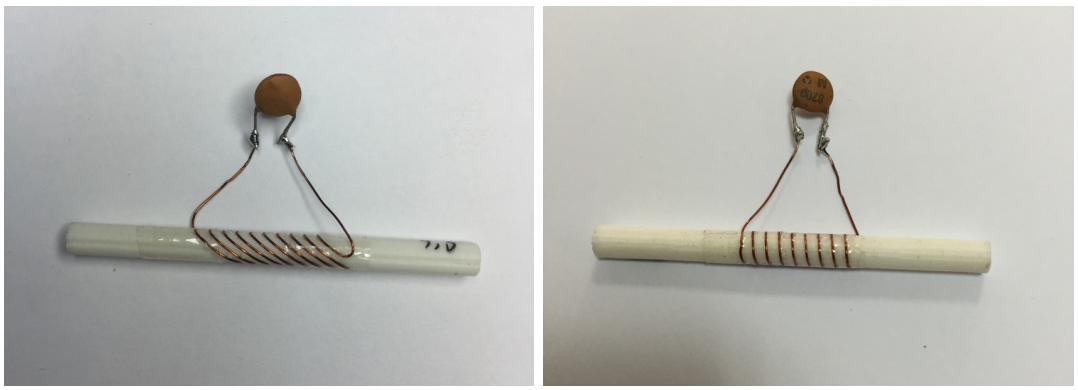

(a) Tilted helical coil (b) Straight helical coil

Figure 4.7. Assembled LC circuits with coils and 820 pF ceramic capacitance.

4.3.1. Tilted Helical Coils

Two type of template core which are different in diameters had been used to fabricate the tilted helices. 6 tilted helical coils were fabricated with 10 mm diameter and different number of turns, N. Similarly 7 different tilted coils were fabricated with 5 mm diameter. Each coil was soldered to 820 pF standard capacitor to form an LC resonator, and its magnetic and electrical characteristics were observed via the non-conducting search probe.

When the tilted coils were inserted inside the circular loop of the non-conducting search probe such that the tilting axis was perpendicular to the loop axis of the probe,

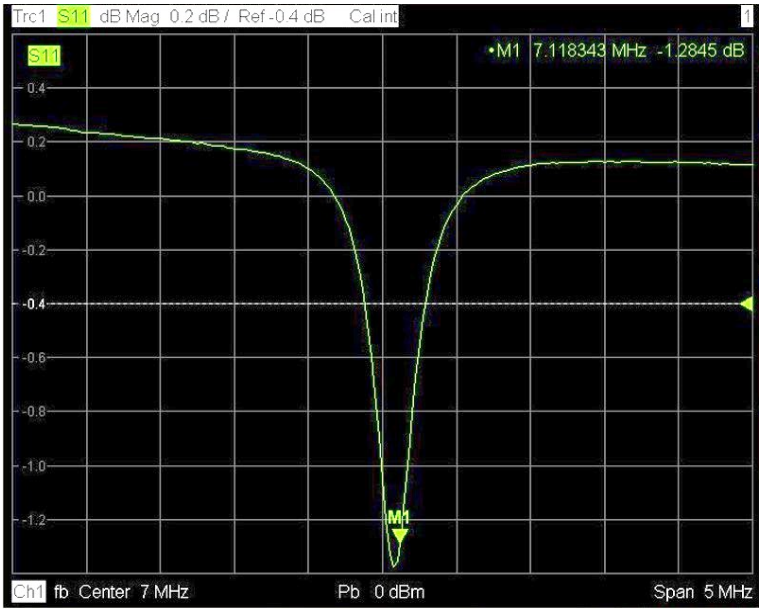

Figure 4.8. Resonance frequency caption for 8.5 turn and 10 mm diameter coil.

a sharp reduction in S_{11} was observed. Arranging the center frequency and span of the plot, the resonance effect was clear to notice. Figure 4.8 shows the S_{11} dB magnitude plot for the coil having 8.5 turn and 10 mm diameter. The resonance frequency was around 7.11 MHz, and more than 1.2 dB fall was the case for this coil. Since the measurement was performed on the non-conducting search probe, the dB fall only shows a qualitative response, not a quantitative value. Therefore, it is possible to observe the bandwidth, directivity of the coil design and the relative quality factor change, but this method does not directly tell the true value of the quality factor.

As the number of turns in tilted helices increased the measured resonance frequency decreased and the inductance value increased. This was an expected behaviour, since the generated magnetic field increases with the additional wirings. The extracted values for 10 mm diameter tilted helical coils showed that there is a linear relation between the number of turns and inductance value. The extracted inductance data from measurements were transferred to MATLAB, and linear interpolation method was used with this data to plot the observed linear relation. Figure 4.9 shows the measurement data for tilted helical coils of 10 mm diameter, and the linear dependency of inductance

with respect to number of turns of tilted coils. For 10 turn coil with 10 mm diameter and 20 mm length the inductance was measured as 643.87 nH. And for 2.5 turn coil with 10 mm diameter and 5 mm length the inductance was measured as 148.71 nH.

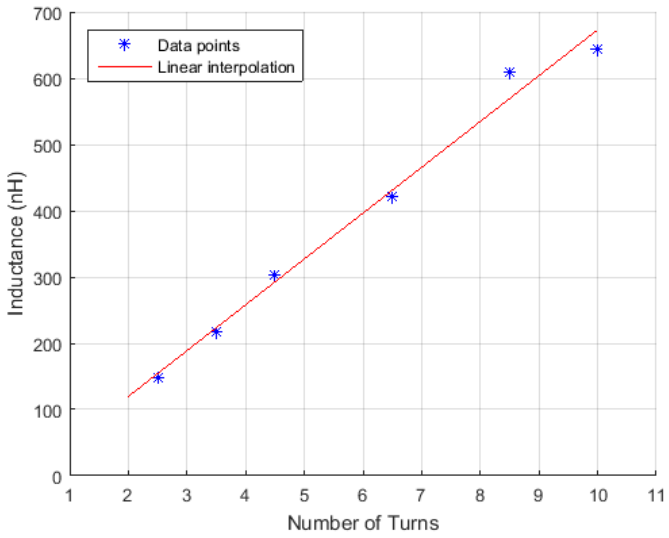

Figure 4.9. Measured inductance values for 10 mm diameter tilted helical coils.

The other 7 fabricated tilted helical coils with 5 mm diameter also repeated the linear dependency. As the number of turns increased, the inductance also increased. This additional data further stated the linear increase in inductance by changing turn number while keeping the pitch between turns and diameter of the coil constant. For 10 turn coil with 5 mm diameter and 20 mm length the inductance was measured as 218.16 nH. And for 2.5 turn coil with 10 mm diameter and 5 mm length the inductance was measured as 75.34 nH.

4.3.1.1. Observed Effects of Diameter Change for Tilted Coils. Figure 4.10 shows the measured tilted helix inductances with their corresponding linear dependencies to number of turns. The measurements show that as the coil diameter decreases, the inductance also decreases. This is another expected results. The magnetic field inside the elliptical loop of the tilted helix increases as the wire diameter increases, although the dependency of inductance to coil diameter change is not directly linear as the case of number of turns. The increasing diameter of the tilted helix increases the inductance.

However, as the number of turns increases this diameter change is further expanded. Therefore, it is possible to introduce a relative effect of number of turns on diameter change effect.

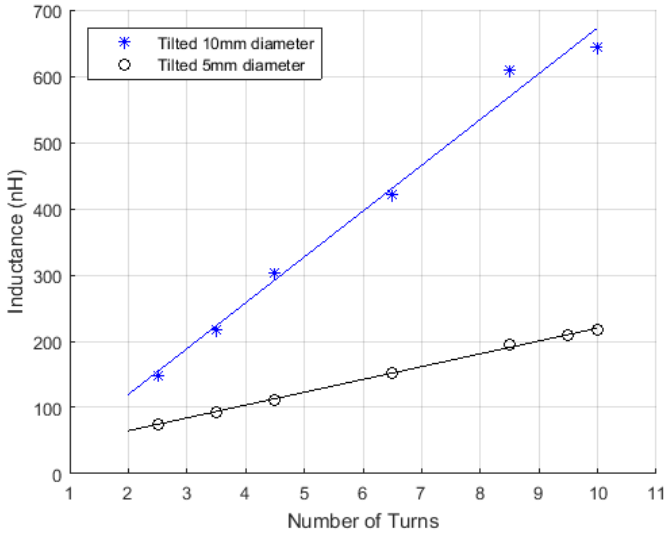

Figure 4.10. Measured inductance values of tilted helical coils.

A further observed effect of diameter change for tilted helical coils was the change on the S_{11} dB magnitude behaviour. As diameter decreased the observed drop on the return loss also decreased. Depending on this fact, it can be concluded that the maximum excitement changes parallel to diameter reduction. Figure 4.11 shows the S_{11} decibel magnitude response measured with vector network analyzer for 10 mm and 6.5 turn tilted coil. The maximum drop at resonance frequency were tried to be obtained by observing the change on the plot while changing the alignment of the coil with respect to the non-contact search probe. For tilted helical coils, this alignment is obtained where the tilt angle is formed in between coil axis and search probe axis.

$$Q = \frac{f_c}{\delta f} \tag{4.2}$$

The bottom point at the drop curve was measured around -1.3 dB with a center frequency of 8.57 MHz. The half power bandwidth was about 0.4 MHz. Figure 4.12 shows the result of the measurement for 5 mm and 6.5 turn tilted coil. This time the bottom point at the drop curve was measured around -0.9 dB with a center frequency of 14.30 MHz. The half power bandwidth for this measurement was around 0.9 MHz. The quality factors for those measurements can be calculated with the Equation 4.2, by taking the qualitative measurement data into account. It was calculated that quality factor for 10 mm 6,5 turn coil was 21.43, whereas it was 15.89 for the coil having same turn number but 5 mm diameter.

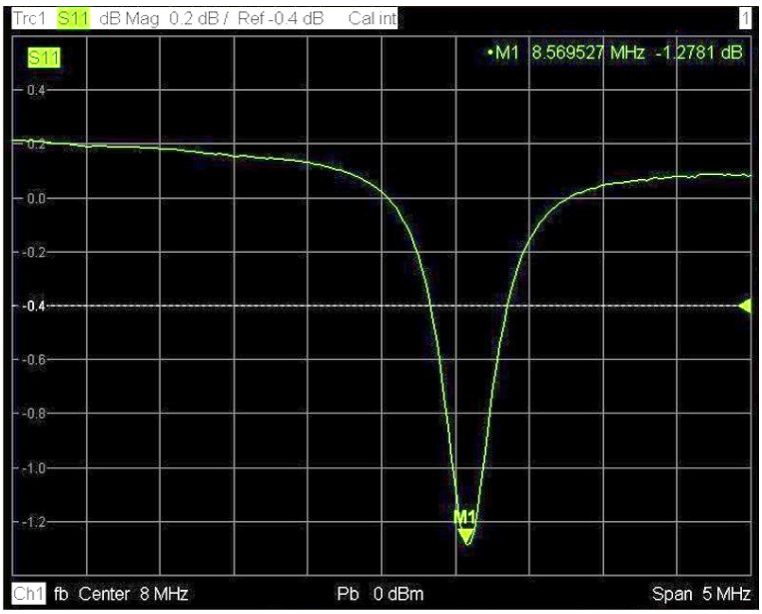

Figure 4.11. Resonance frequency caption for 6.5 turn 10 mm tilted helical coil.

It was clear that, tilted helical coils with higher dimension provide higher quality factor and S_{11} drop at their respective resonance frequency. This was an expected behaviour, since the inductance values get higher for the tilted helices as their diameter increases, while number of windings stay the same. And higher inductance is a direct result of improved magnetic power.

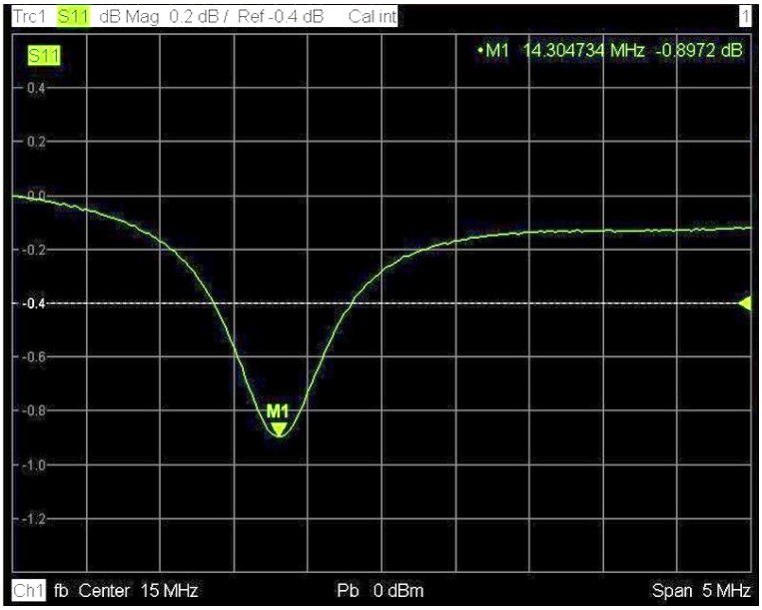

Figure 4.12. Resonance frequency caption of 6.5 turn 5 mm tilted helical coil.

4.3.2. Straight Helical Coils

The parameters were held almost identical to tilted helices in order to provide a proper comparison for the effect of introducing a tilting angle to coil structure. Two type of template core which were different in diameters had been used to fabricate the straight helices. 6 straight helical coils were fabricated with 10 mm diameter and different number of turns. Similarly 7 different straight coils were fabricated with 5 mm diameter. Each coil was soldered to 820 pF standard capacitor to form an LC resonator, and its magnetic and electrical characteristics were observed via the non-conducting search probe.

When the straight coils were inserted inside the circular loop of the non-conducting search probe such that the coils were perpendicular to the loop axis of the probe, again a sharp reduction in S_{11} was observed. The resonance effect was clear to notice, and the center frequencies were arranged for each measurement. Figure 4.13 shows the S_{11} dB magnitude plot for the straight coil having 8.5 turn and 10 mm diameter. The resonance frequency was around 8.98 MHz, and more than 2.5 dB fall was measured.

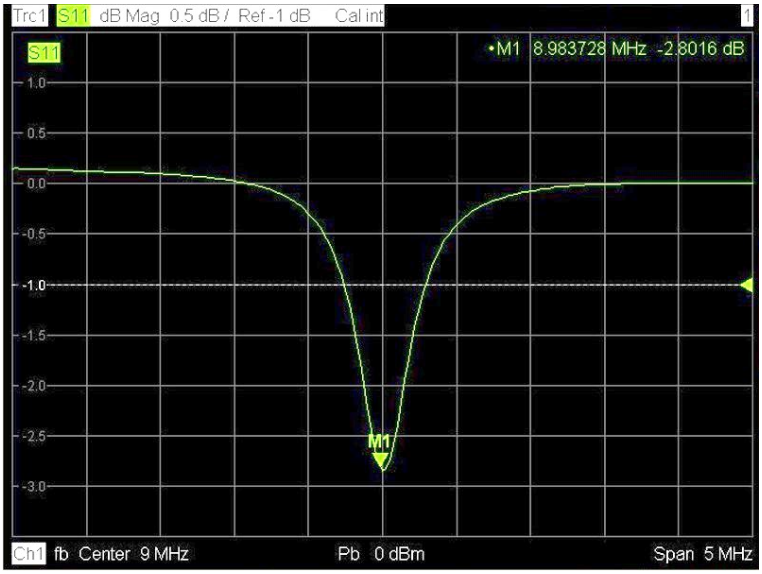

Figure 4.13. Resonance frequency caption of 8.5 turn 10 mm straight helical coil via vector network analyzer.

As the number of turns in straight helices increased the measured resonance frequency decreased and the inductance value increased. This was a common and expected behaviour for straight helical coils. The extracted values for 10 mm diameter straight helical coils showed that there is again a linear relation between the number of turns and inductance value. The steps to create the plots for measured data repeated for straight helical coils. The extracted inductance data from measurements were transferred to MATLAB, and linear interpolation method was used with this data to plot the observed linear relation. Figure 4.14 shows the measurement data for straight helical coils of 10 mm diameter, and the linear dependency of inductance with respect to number of turns of straight coils. 6 different tilted helical coil designs with same diameter but changing number of turns were used to generated plot data. The linear interpolation also achieved with the help of those 6 data points, obtained with finite element method simulations. The results were all in nH range. For 10 turn coil with 10 mm diameter and 20 mm length the inductance was measured as 431.02 nH. And for 2.5 turn coil with 10 mm diameter and 5 mm length the inductance was measured as 111.54 nH.

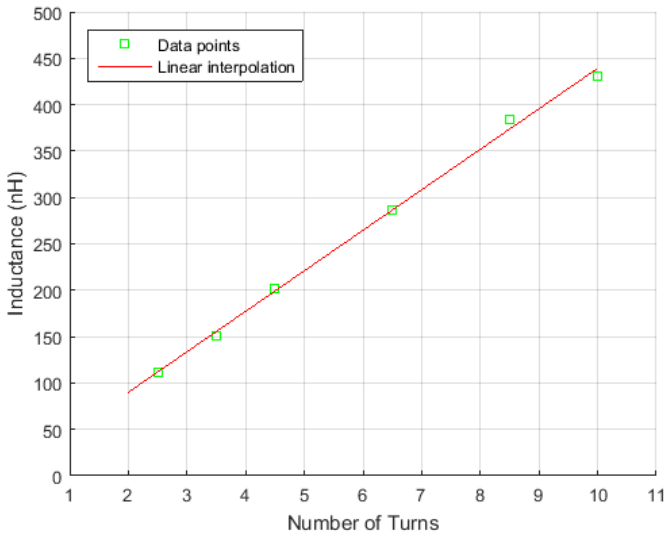

Figure 4.14. Measured inductance values for 10 mm diameter straight helical coils.

The results for the other 7 fabricated straight helical coils with 5 mm diameter again repeated the linear dependency. As the number of turns increased, the inductance also increased. This additional data further stated the linear increase in inductance by changing turn number while keeping the pitch between turns and diameter of the coil constant for straight helical coils. For 10 turn straight coil with 5 mm diameter and 20 mm length the inductance was measured as 156.87 nH. And for 2.5 turn straight coil with 10 mm diameter and 5 mm length the inductance was measured as 51.12 nH.

4.3.2.1. Observed Effects of Diameter Change for Straight Coils. The collected measurement data for all straight helical coils were plotted in Figure 4.15, with changing diameter. The data for straight helices points that as the coil diameter decreases, the inductance also decreases, which was also the case for tilted helices. The magnetic field inside the circular cross section of the tilted helix increases as the wire diameter increases, although the dependency of inductance to coil diameter change is not directly linear as the case of number of turns. The increasing diameter of the straight helix takes the inductance value higher. However, as the number of turns increases the amount of the change in inductance also goes higher. It is not possible to define a direct relation of diameter on inductance regardless of number of turns in the coil.

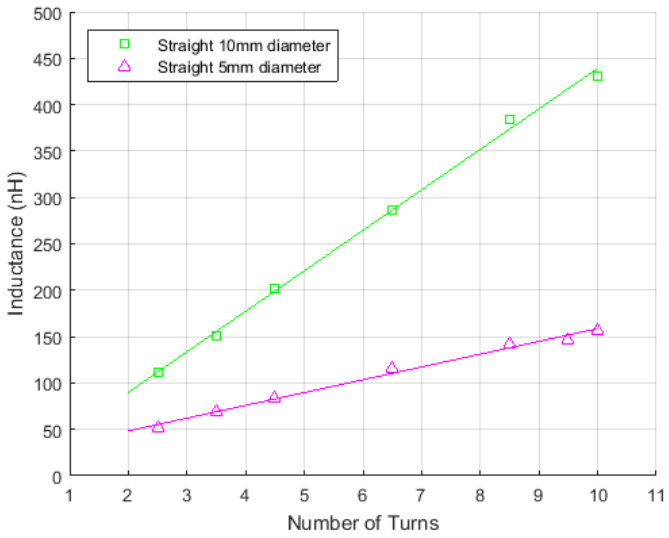

Figure 4.15. Measured inductance values of straight helical coils.

As diameter of straight helical coils changes the peak point of the magnitude on the drop of S_{11} was effected in addition to inductance change. The decrease in the diameter of the straight coils also reduced the magnitude of S_{11} drop at resonance frequency. A direct relation was the case for this parameters. Figure 4.16 shows the S_{11} dB magnitude response measured with vector network analyzer for 10 mm and 6.5 turn straight helical coil. The maximum drop at resonance frequency were tried to be obtained by observing the change on the plot by keeping the coil perpendicular to the z-axis of the non-contact search probe. The bottom point at the drop curve was measured around -2.8 dB with a center frequency of 10.38 MHz. The half power bandwidth was about 0.5 MHz. Figure 4.17 shows the result of the measurement for 5 mm and 6,5 turn straight helical coil. This time the bottom point at the drop curve was measured around -0.65 dB with a center frequency of 16.32 MHz. The half power bandwidth for this measurement was around 1.5 MHz. It was calculated that quality factor for 10 mm 6.5 turn straight coil was 20.76, whereas it was 10.88 for the straight coil having 5 mm diameter.

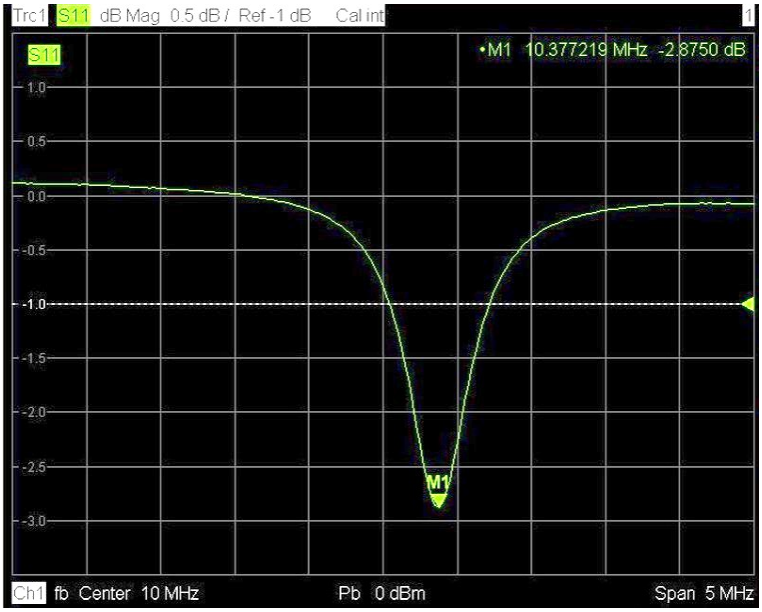

Figure 4.16. Resonance frequency caption of 6.5 turn 10 mm straight helical coil.

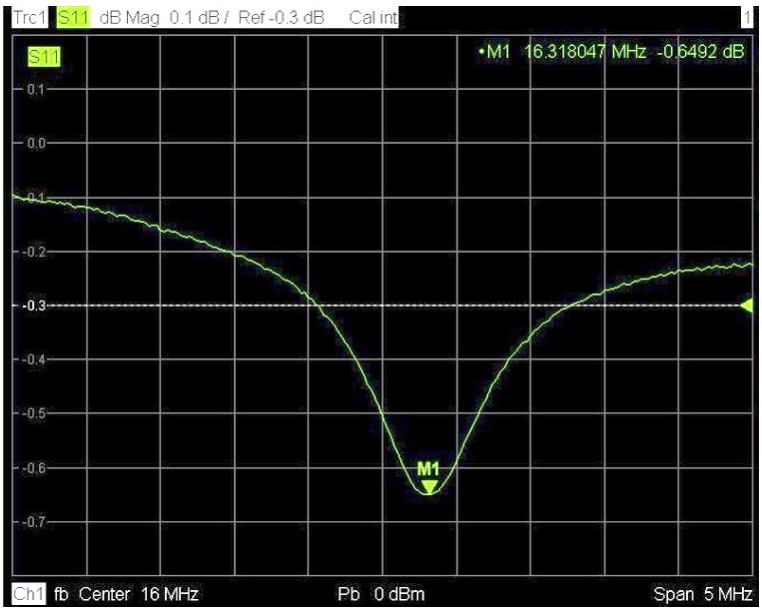

Figure 4.17. Resonance frequency caption of 6.5 turn 5 mm straight helical coil.

4.3.3. Comparison of Tilted and Straight Helical Coils Measurements and Directivity

Having the same dimensions and identical turn numbers, introducing a tilted angle to helical coil structures improved the magnetic behaviour and resulted into higher inductance values. Figure 4.18 shows complete measurement data for tilted and straight helical coils. The maximum inductance value among the fabricated samples was observed with the tilted helical coil which has largest diameter and turn number. The minimum value obtained with the straight helical coil which has the smallest diameter and minimum turn number. It was a noticed effect that the quality factor declined as inductance value decreased. The highest S_{11} drop was observed with the coil having highest inductance.

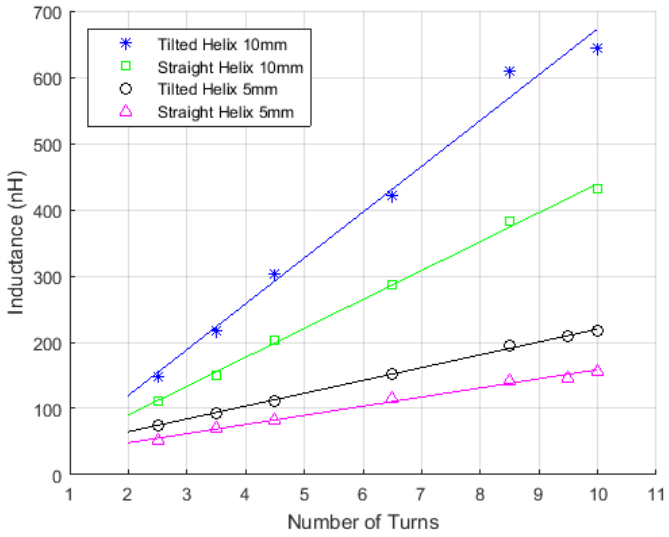

Figure 4.18. Complete measured inductance values of coils.

In Figure 4.19, the directionality characteristics of straight and tilted helices were stated out. The coils were aligned in different angles with respect to the z-axis of the circular loop of the search probe. Perpendicular, parallel, and tilt angle orientations were measured. The maximum and minimum drops for straight and tilted helical coils having 10 turn and 10 mm diameter noted. It was noticed that the maximum drop off S_{11} was measured for straight helix when its longitudinal axis was parallel

to the circular loop z-axis. -3.5 dB drop was noticed for this case. Almost no drop was observed when it was placed perpendicularly to the circular loop. For the case of tilted helix, the maximum excitement was obtained when its tilting angle was formed in between z-axis of the circular magnetic field generating loop and the coil. -4.4 dB drop for S_{11} indicated the highest excitement noticed among the fabricated samples. For tilted helices, whatever the angle between coil and circular loop was, there was always a certain drop on S_{11}. Even with parallel placement, more than 1.5 dB drop in magnitude was measured. This proves the directionality of tilted helix has wider distribution in 3D than straight helix. There was not uniformity in directional response for single layer tilted coil, but double tilted helix design can improve transverse plane uniformity with the help of a second tilted helix winding on top of the first one.

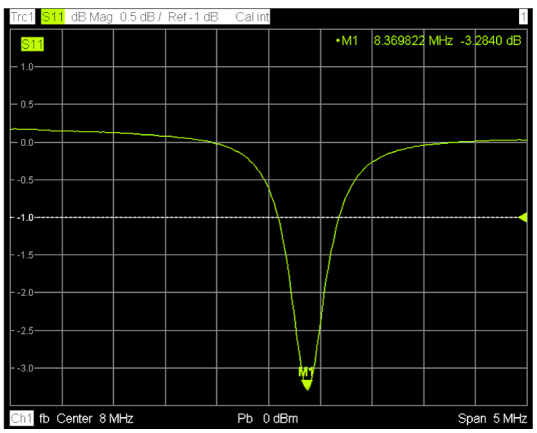

(a) Straight coil - perpendicular

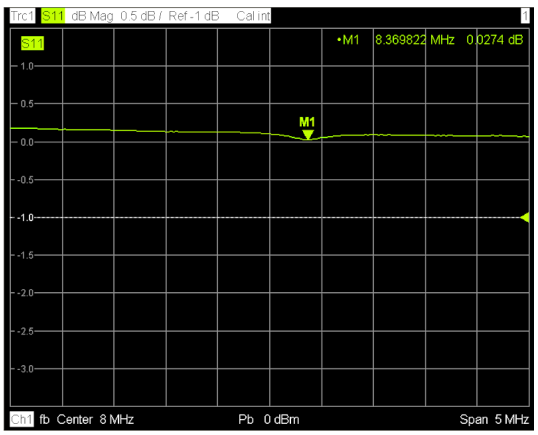

(b) Straight coil - parallel

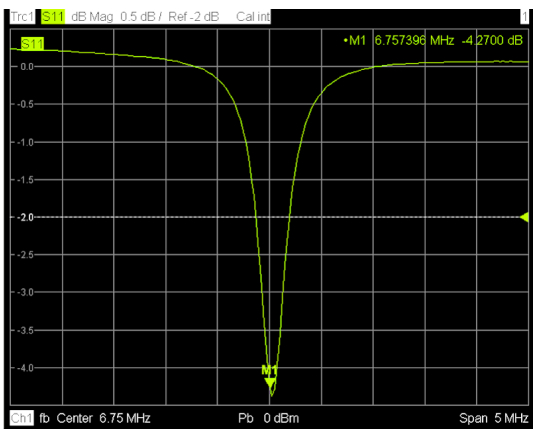

(c) Tilted coil - tilt angle

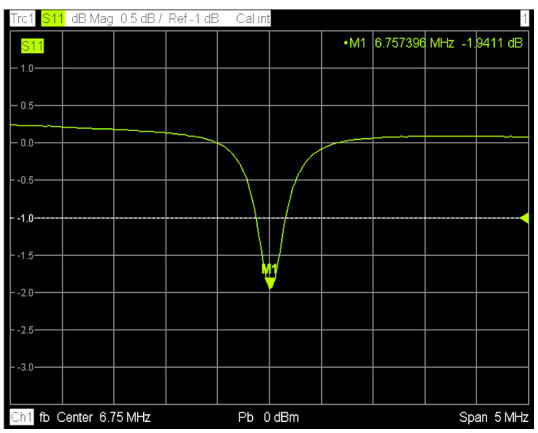

(d) Tilted coil - parallel

Figure 4.19. Directionality captions of tilted and straight helical coils.

4.4. Comparison of Simulations and Measurements

Complete inductance values obtained for all samples by simulations and measurements, and their respected linear dependencies on number of turns are stated in Figure 4.20. The results of simulations and laboratory measurements are parallel to each other. For coils with smallest dimensions the results are almost identical, and as dimensions get larger the margin of error increases. However, the general behaviours are the same for both simulations and measurements. There is no unexpected differentiation or considerable errors. The initial trials for both simulations and measurements had higher margin of errors, which was because of not including some physical parts in geometry for simulations. Using the same dimensions and structures both in simulations and fabrications has provided congruent data.

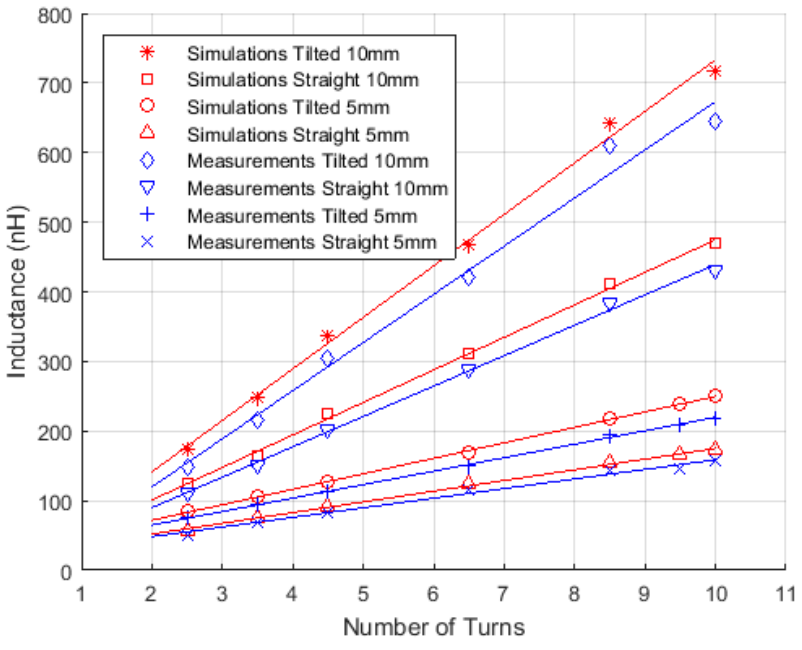

Figure 4.20. Inductance results of simulations and measurements.

In Figure 4.21 the simulation results for magnetic field of straight and helical coils are presented. Parallel to directionality measurements, straight helical coils has strong magnetic fields through the normal vector of their curvature, but a change in the direction causes significant drop in magnetic field. On the other hand, tilted helical

coils have a peak magnetic field on the surface of curvature and its magnitude also reduces as direction changes. However, the reduction of magnetic field due to change of direction is less severe in tilted helical coils than straight helical coils. These features of the coils are also presented in Figure 4.19 of measurements. Comparing the plots of inductance and magnetic field of simulations and measurements together, it is clear that the FEM simulations are reliable for coil simulations in order to express their magnetic and electrical properties.

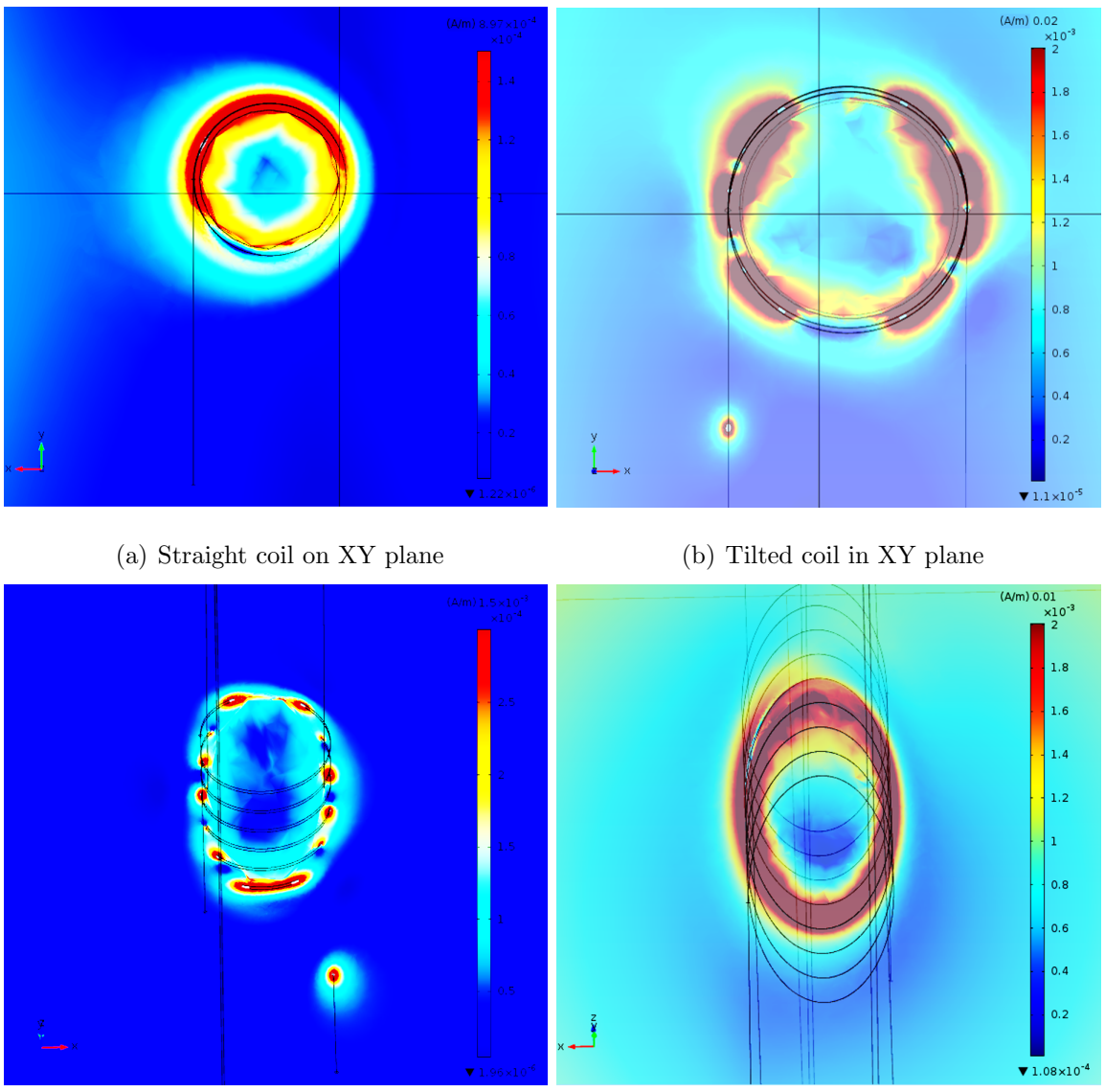

(a) Straight coil on XY plane

(b) Tilted coil in XY plane

(c) Straight coil on tilting plane

(d) Tilted coil on tilting plane

Figure 4.21. Directionality simulations of tilted and straight helical coils.

5. MRI RECEIVER COIL DESIGN FOR 5 FR CATHETER

In Chapter 3, designs and FEM simulations for helical coil structures were studied. Following this step, fabrications of simulated coil structures were accomplished and measurements were done using the vector network analyzer. The comparison of simulation and measurement steps revealed the reliability of FEM simulation tools. And now they are ready as convenient tools to design the optimum receiver coils prior to fabrications, reducing the total time spent significantly. Relying on the simulation platforms, in this Chapter and introductory tilted double helix receiver coil for MRI applications was designed and studied. High Frequency Structural Simulator (HFSS) is used to analyse the characteristics of the model. Following this work, the fabrication of simple LC resonators on 5 Fr catheter by using lithography took place. This LC resonator coil was tuned closer to 63.8 MHz frequency, and MRI tests were performed. The resonator structure was monitored under MRI.

5.1. Geometry and Circuit Modelling

The simulations and measurements pointed out that the magnetic directionality characteristics of tilted helical coils are wider in such a way that they can generate magnetic field in all 3 axes, or they can be easily excited with external magnetic pulses from all directions. However, the magnetic field of tilted helical coil is maximum at the center of the tilt plane, and reduces on the other directions. In order to improve the magnetic field at the directions other than tilt axis and to provide enhanced uniformity in 3D, a second tilted helical coil is winded on the first one with reversed tilting angle. This structure is called as tilted double helix. The RF signal is transferred between layers with the help of additional capacitor designs. The combined system results in a complex LC resonator. By connecting these ports to an external monitoring system, it is possible to use the device as active monitoring tool. And connecting these 2 ports together will create a passive monitoring device for MRI applications.

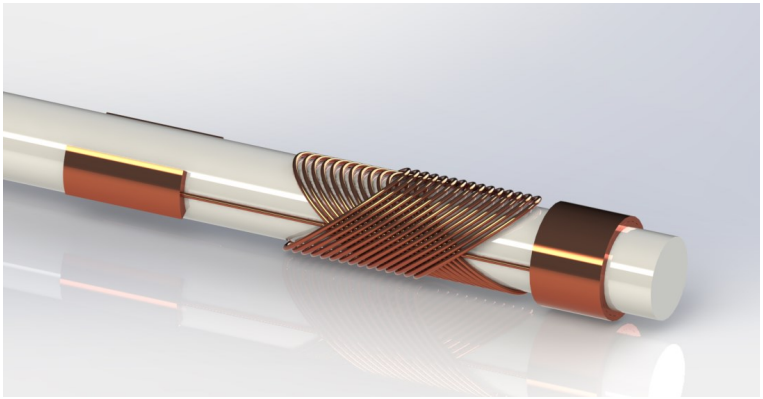

Figure 5.1. Designed double helix catheter structure for MRI.

5.1.1. Circuit Modelling

The tilted double helix receiver design is mainly composed of inductive and capacitive elements. Figure 5.2 shows these elements on 3D view of the structure. The tilted helices of inner and outer layer are magnetic field generating components and they are the main source of the visualization under MRI. As an active catheter monitoring device, the AC signal is introduced over $Port_1$ and $Port_2$. As signal goes through L_{outer}, which is a tilted helical coil, it generates a strong magnetic field around the first tilting axis. The signal reaches the ring capacitor C_{ring} near the edge of the 5 Fr catheter, and this capacitive element transfer signal to inner layer over the insulating layer. The AC signal then goes through L_{inner}, generating a second magnetic field around the respective tilting axis. Through the rectangular capacitor C_{int}, which is wrapped over the surface of the catheter, signal reaches to $Port_2$. The structure between two ports acts as a complex LC resonator.

In Figure 5.3, the extended circuit modelling is presented. In this model the electrical characteristics of inductors are taken into account by modelling them as RLC circuits. On the other hand it is possible to neglect the effects of R_{coil} and C_{coil} elements for MRI frequency band which is 64 MHz, since the resistance values of coils are low enough to be neglected due to the small total conductor length and the minor capacitance values make the elements acts as open circuits. Therefore, by

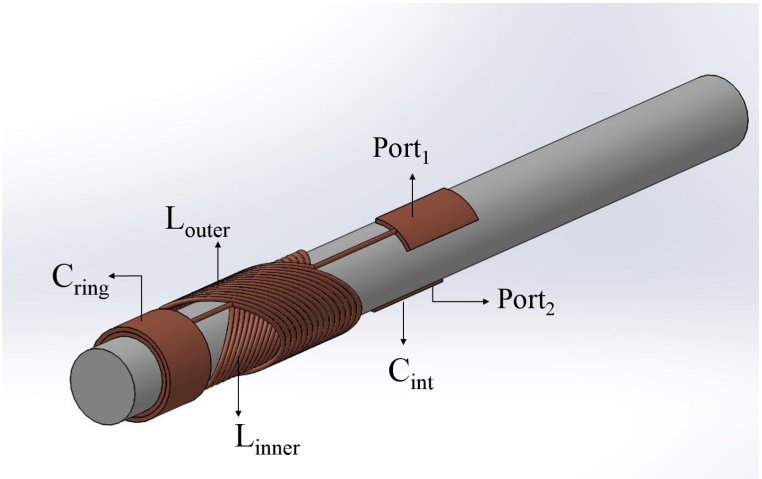

Figure 5.2. Structural elements of the double helix resonator.

taking out those R and C elements, the model can be simplified. $C_{overlap}$ is the artificial capacitance formed by the overlapping windings of tilted helices, and represented here as a series of inductors and capacitors together with L_{inner} and L_{outer} to model is at small overlapping capacitor values. It is modelled here with 4 capacitors, but the real number is equal to the number of every intersection areas between coils. C_{ring} and C_{int} should be designed in a way that the capacitive effect of $C_{overlap}$ can be suppressed by those 2 large capacitance. Therefore, an easy mathematical model for the tilted double helix receiver structure can be conceived. This simple model can be seen in the schematic which is stated in Figure 5.4.

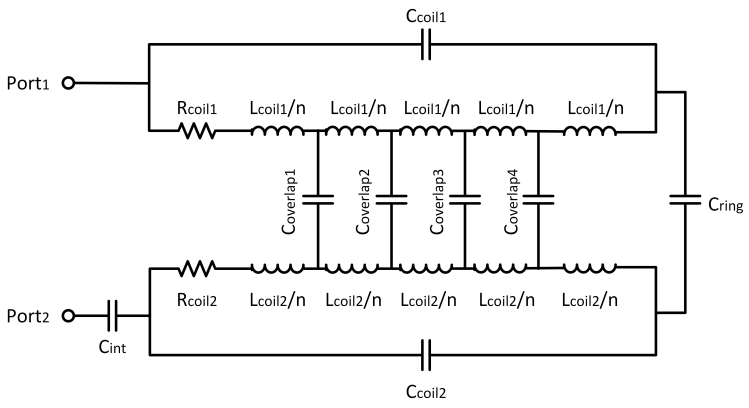

Figure 5.3. Electrical model of the catheter device.

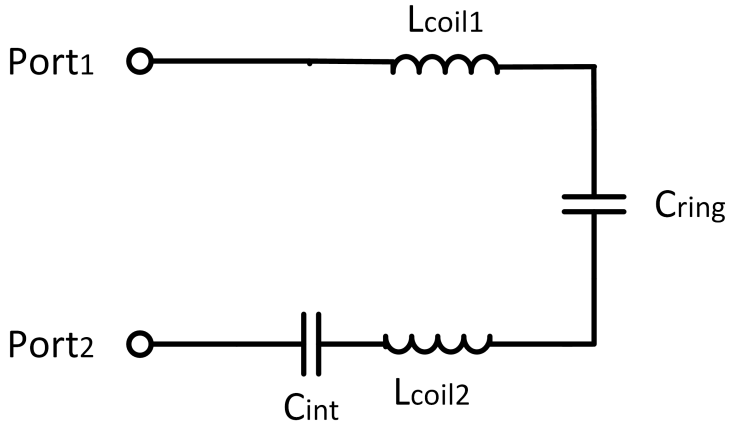

Figure 5.4. Simplified electrical model of the catheter device.

5.1.2. Ring Capacitor

The ring capacitor is formed by two overlapping cylindrical conductor layers and a parylene layer as insulator in between. The thickness of the conductor layers are 100 μm, and there is 5 μm thick parylene layer in between as insulator. The longitudinal dimension of the cylindrical pads is 1 mm. The radius of the center of the insulating layer can be used to calculate the mean area of the pads, which will then be used to find the capacitance value. Equation 5.1 expresses the derivation of mean radius of C_{ring}.

$$r_{mean} = \frac{D_{cylinder}}{2} + t_{wire} + \frac{t_{insulator}}{2} \tag{5.1}$$

In this equation, $D_{cylinder}$ is the catheter diameter, t_{wire} is wire thickness and $t_{insulator}$ is the parylene layer thickness. Using this mathematical expression the mean radius, r_{mean}, is found as 0.9350 mm. The capacitance was found as 3.12 pF with these values with Equation 5.2. The parasitic effects near the edge of this ring capacitor were neglected.

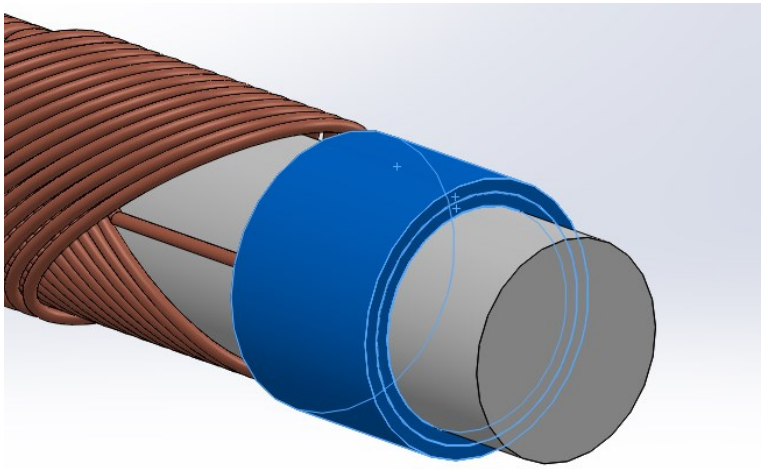

Figure 5.5. Ring capacitor.

$$C = \frac{\epsilon_r \epsilon_0 A}{d} \tag{5.2}$$

5.1.3. Intermediary Capacitor

Since the structure is composed of 2 layers, the signal provided from the outer layer transmitted to inner layer through the ring capacitor. Passing through the inner tilted helix, the signal reaches to contact pad of the inner layer. In order to take signal to $Port_2$ which is located at the outer layer another capacitor is needed to be designed at this point. At the top of the pad of the inner layer another pad is placed, and the parylene layer in between acts as an insulator layer to form a capacitance with these 2 pads. The length of pads is 2.50 mm, and it is formed by an arc around the cylinder with the same mean radius of ring capacitor, which is 0.9350 mm. The mean area of pads is calculated as 2.45 mm^2, and the capacitance is found as 1.30 pF.

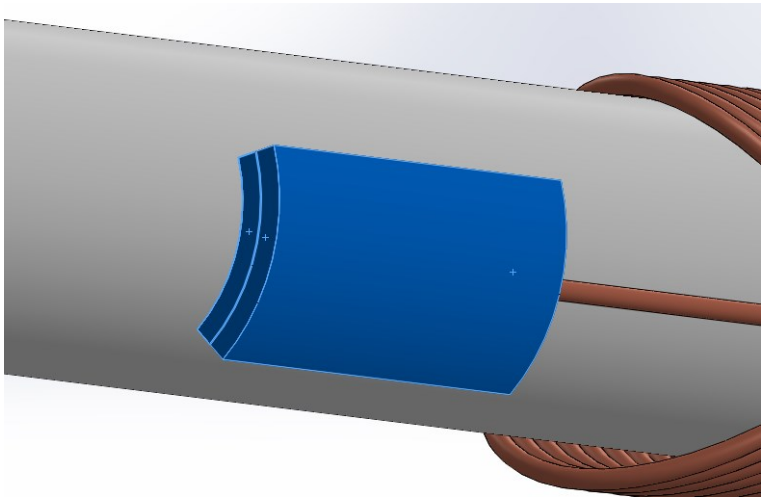

Figure 5.6. Intermediary capacitor.

5.1.4. Overlap Capacitor

The overlap capacitor is a side effect of helix windings. The intersection area of wires acts as an artificial capacitor, having conductor parts of wires as capacitor pads, and the thin insulator layer as dielectric material of capacitance. Each intersection area acts as a separate capacitor, and this situation also divides each inductor to small coil pieces. Therefore, the overlap capacitor should be modelled as a set of capacitor connecting each small inductor part to the other layer. In the first circuit model, the overlap capacitor is represented with 4 capacitor and respective inductor parts, but the actual number is higher than this representative number. Actual number can be obtained by calculating the number of cross section areas. Each inductor was designed to have 15 turns of winding. The square of this number gives the number of capacitors at each side of the catheter, which make 225 on each, and in total 450. At the top and bottom parts, there are additional intersection areas. However, their cross-sections are higher than the others. Therefore, they have to be separately calculated. In order to estimate the effect of this overlap capacitor, different approaches were tried. The perpendicular center planes of wires first thought to be used as the capacitor planes in calculations. However, taking the fact of most of the current flows through the surface of conductors into account this approach was disproved. The expected capacitance

effect of the overlap capacitor is not considerable. Therefore, the idea of performing the calculations by neglecting this capacitive effect, and extracting it from the simulation results was actualized.

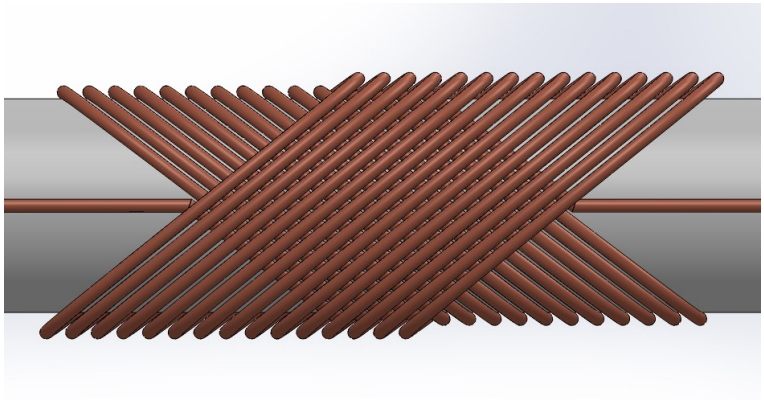

Figure 5.7. Overlap capacitor.

5.1.5. Tilted Helical Coils

Tilted helices are the magnetic field generating components of this catheter receiver structure. The expected excitation in the coils due to RF magnetic pulse at 63.8 MHz for 1.5T MRI systems will produce image. As the inductance value gets higher the excitement of the coils becomes higher in magnitude. Therefore, the resulted image is clearer under MRI. Increasing number of turns, closer pitches multiplies the quality factor of the coil response as it is clear from the simulations and measurements. For this purpose the tilted coils were first designed such that each had 15 turns of 100 μm wire with 100 μm pitch. The capacitance geometries first designed to match this inductors to 63.8 MHz. During the simulation step, due to the memory dependent computational problems the designs were rearranged and updated for lower turn number coils and related capacitance geometries. The wire and pitch dimensions stayed the same, but helices designed with 5 turns of windings. The capacitance geometries ,which were mentioned in earlier sections, were the final designs for this new turn number.

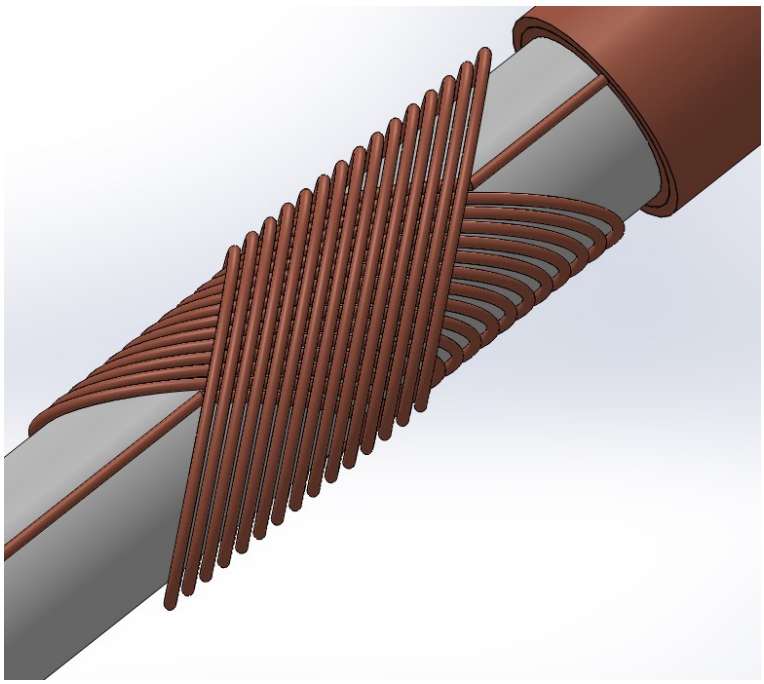

Figure 5.8. Tilted helices.

5.2. HFSS Simulations

Simulations of tilted double helix resonator were achieved via HFSS program. The geometrical model was recreated on this program with the same parameters and dimensions. Materials were assigned for conductor and insulator parts. The surrounding material was defined as air for this simulations. Meshes were built for each part of the structure, and especially for wire and insulator parts very thin small tetrahedral meshes were generated. Current was introduced from one port pad, and electrical and magnetic field studies were defined. Due to high mesh number the iterative solvers consumed about 52 GB of RAM during the simulations, and the total used time to complete the simulations was approximately 112 hours and 47 minutes. The magnetic field within and around the resonator were plotted in 3D, as well as electrical parameters such as inductance, S_{11}, and $VSWR$. In Figure 5.9, the magnetic field within the geometry was plotted in 3D. Figure 5.10 shows the magnetic field within and around the catheter structure.

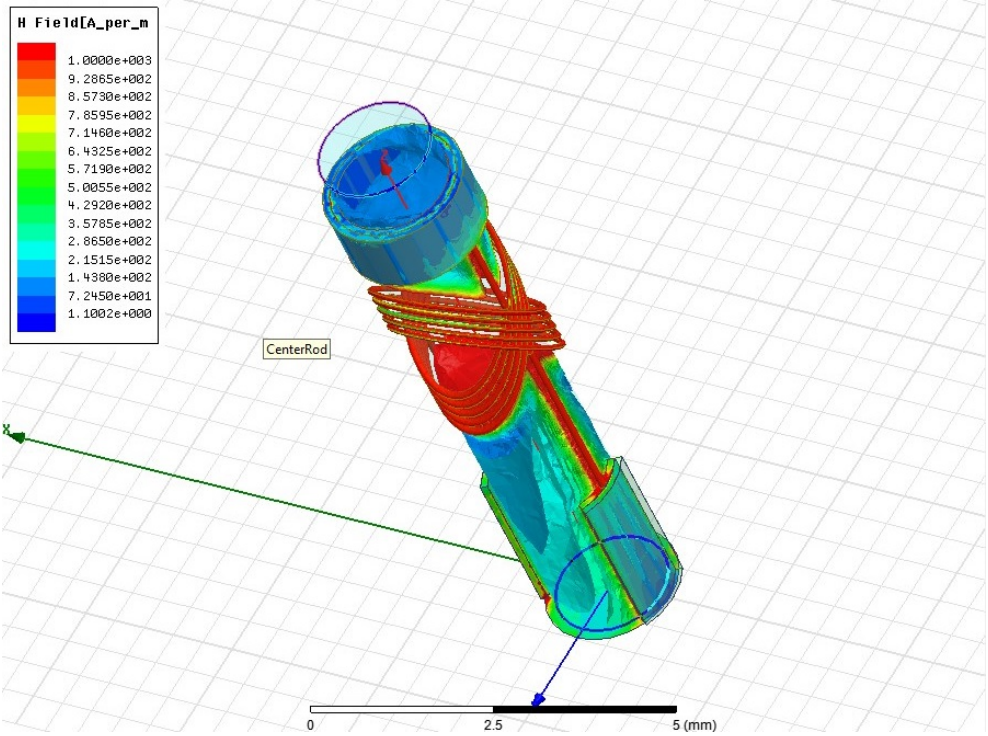

Figure 5.9. Magnetic field inside the geometry.

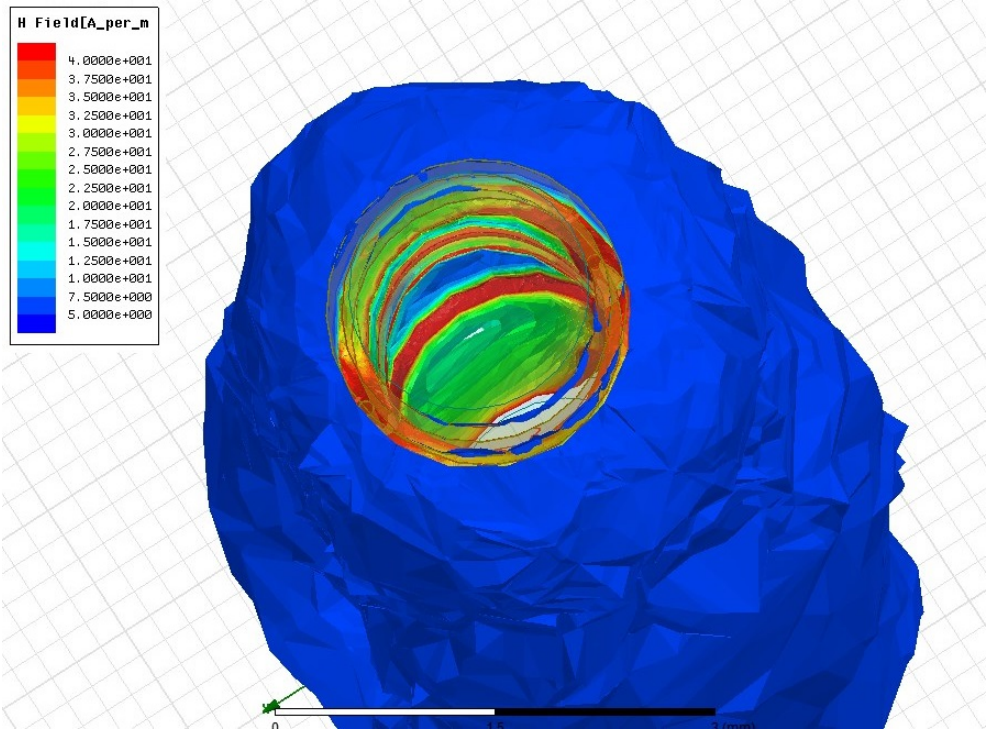

Figure 5.10. Magnetic field around the catheter.

The frequency response of S_{11} dB magnitude was plotted in Figure 5.11. The resonance frequency was observed around 62.74 MHz, which was 1.06 MHz away from the design frequency that was 63.8 MHz. That is a very close result to hand calculations which were made before designing the structure geometry. The inductance plot in Figure 5.12, also shows the effect of resonance at the same frequency.

There is a main reason of resonance frequency difference from the initial design frequency which is the neglected effect of the overlap capacitor, and other capacitive and resistive components of inductors. The complex circuit representation of design and following that the mathematical derivation of resonance frequency were tried to be simplified by ignoring those elements. Therefore, it was not expected to have the exact results with the theoretical calculations. On the other hand, the results are still very close to the designed values.

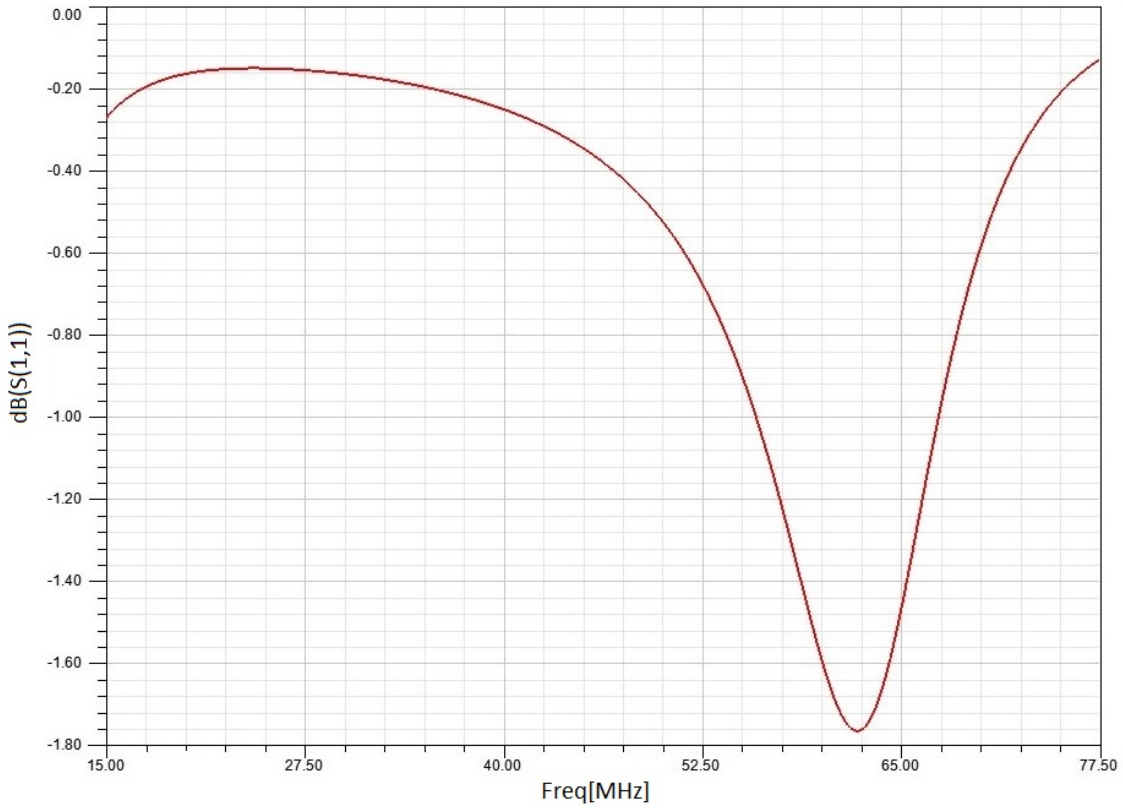

Figure 5.11. S_{11} plot of the structure.

The drop of S_{11} at the resonance frequency was around 1.8 dB. That was a low

value for MRI applications, and the reason behind this response is the reduced turn numbers that were used to create tilted helical coils. Initial turn number was 15, and this value was reduced, because of excess memory consumption of simulations. This simulation study is just an example to point that the simulation platforms are valid tools to test the designed structures and to demonstrate the physical effects. The actual tilted double helix catheter tip design will include helical coils having higher number of turns, in order to increase the magnetic strength and enhance the quality factor.

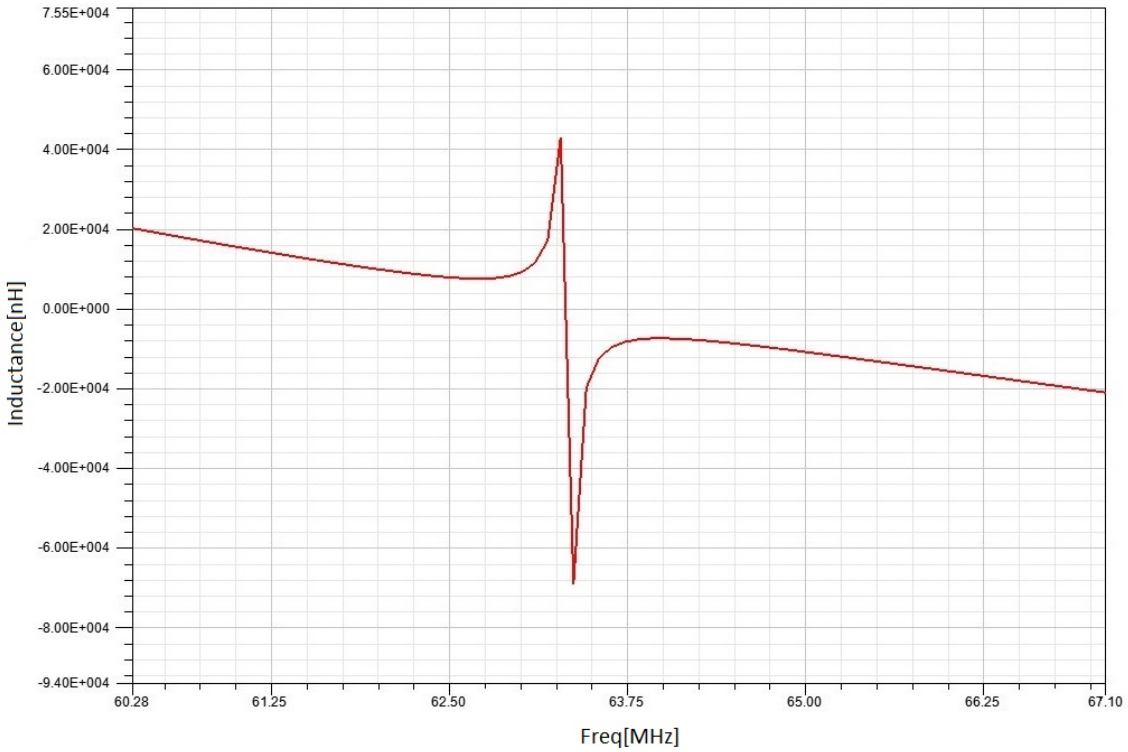

Figure 5.12. Inductance plot near resonance frequency.

The resulted values and plots presented the expected characteristics. Depending on this, the simulation platforms can be used to bring out the optimum catheter tip design. And this was the initial aim of this thesis study, introducing the computational tools and FEM simulators to reduce the overall time spend for blind fabrications, which were being held with test and fail method, in order to create a working device. The structure can be designed and simulated via FEM simulators, and fabrications can be made after creating the desired structure. This approach will improve the quality and effectiveness of research studies.

6. CONCLUSION AND FUTURE WORK

In this thesis study, the characteristics of straight and tilted helical coils were analysed and compared through theory, simulations and laboratory measurements in order to show the consistency and convenience of FEM simulations as a tool to develop interventional MRI catheter coils. 26 tilted and straight helical coils with different geometries were simulated. Those 26 simulated coils were also fabricated at the laboratory for measurements via vector network analyzer. The inductance values, magnetic field directionalities and resonance frequencies were observed and compared. The simulations and measurements provided consistent results, proving the stability of FEM simulations. Once this main objective of thesis study was achieved, an introductory double tilted helical tip design and simulation was carried out for interventional MRI applications with 5 Fr catheter.

The results of this study has indicated that tilted helical coils has improved characteristics for MRI applications when compared to straight helical coils, depending on increased inductance values, wider magnetic field projections on general axes. The inductance values of designed helical coils were on the range of hundred nanohenries, with 270 μm conductor inside 30 μm thick insulator layer. The dependency of inductance on number of windings and radius of curvature for both tilted and straight helical coils were investigated. It has been revealed that inductance of coils has a linear dependency with number of windings, and an increase in radius of curvature results also increase in inductance.

In order to find the resonance frequency through simulations both radio frequency and magnetic field tools were utilized. The fastest method to find the resonance frequency of a coil design was searching eigenvalue near pre-estimated frequencies. Other than that, frequency sweep was enabled to detect the resonance frequency by observing the change in the characteristics structures and plots of the results. There were small difference in the resonance frequencies depending on the used tool. However, they were close enough to state each method was reliable.

The works accomplished in this thesis have verified the convenience and reliability of FEM tools so far. On the other hand, the overall project includes the design and fabrication of passive device as a 5 Fr catheter tip. Apart from this thesis study, fabrication techniques were developed depending on coating of Cr, Au on cylindrical catheter surface, and additional electroplating process in order to form coils and LC structures on catheters. So far LC resonators were created with single layer straight helical windings and a ring capacitors at close to front end of the catheter. After fabrication dimensions were rechecked under microscope, and measurements were carried out with vector network analyzer. This LC structure were first measured to have 69.49 MHz resonance frequency on air, and this value was lower down to 65.49 MHz when measured inside the 0.9% isotonic solution. Figure 6.1 presents the image of resonator structure under microscope.

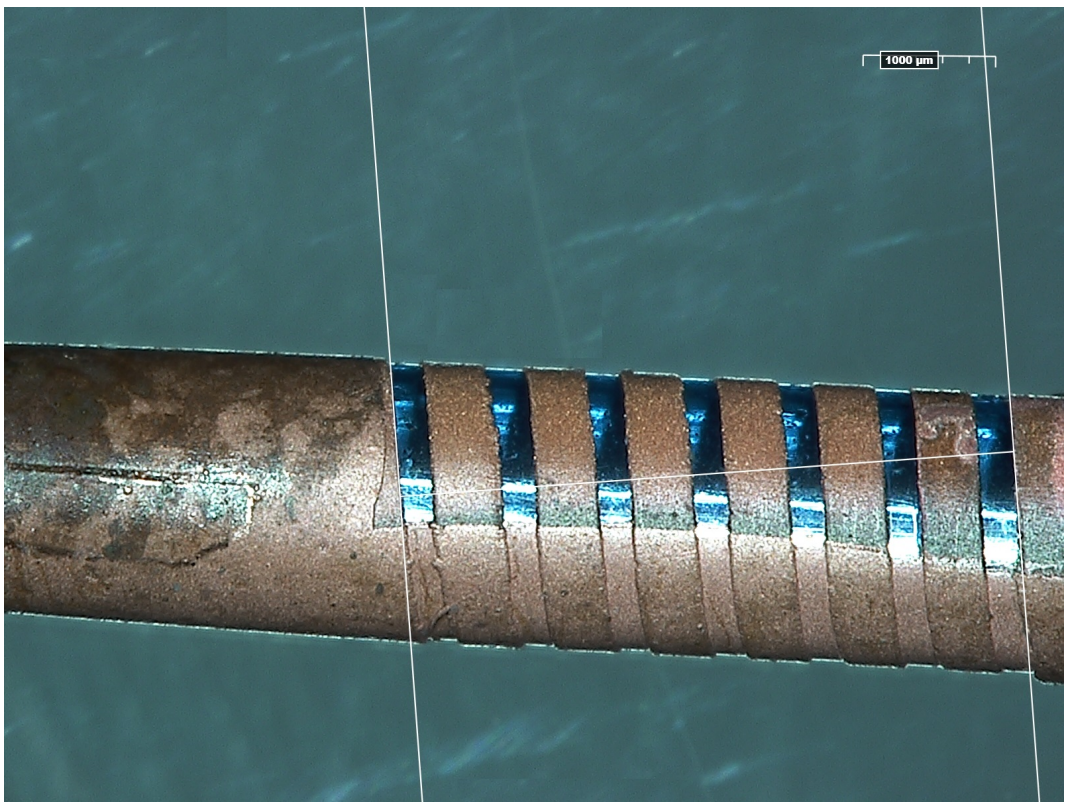

Figure 6.1. LC resonator structure fabricated on 5 Fr catheter.

About 100 nm Cr-Au was coated at first on the catheter surface, and then Cu was electroplated to provide a conducting layer thickness of about 35 μm. Parylene was

then coated on top of this inner layer to create both isolation for layers, and insulating media for capacitor. This parylene thickness was about 2.5 μm. Outer pad of the ring capacitor and a thin straight line was coated in an additional conductor layer via Cr-Au and following Cu electroplating. The purpose of straight conductor line is to create a bridge between the outer pad of capacitor and end of helix windings to form a contact and close the loop of structure. This contact part also creates relatively small capacitor due to 6 small intersection areas with the helix windings. 4100 μm length was provided for contact pad of capacitor and inductor. A final parylene layer was coated for further isolation. The ring capacitor has a length of 5027 μm. The result of the hand calculations for this capacitor is 289.31 pF, and the value of the small contact capacitor as 5.77 pF. The inductance has a length of 4644 μm, and has 7 windings with as an average 250 μm pitch and 470 μm winding. The calculated inductance was 21.30 nH. Resonance frequency was calculated as 63.50 MHz, and the measurements resulted as 69.49 MHz with an error of 8.62% margin of deviation.

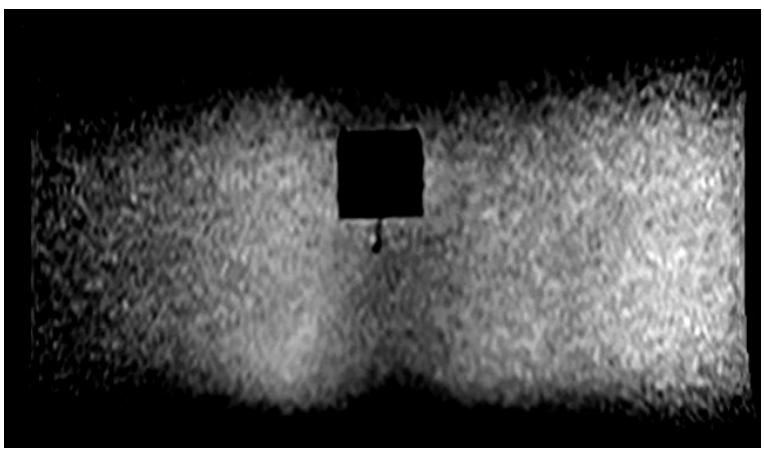

Figure 6.2. MR image of the fabricated LC resonator.

Figure 6.2 shows the image taken under MRI for the coil structure. This study was carried out by the other graduate students to develop fabrication techniques for helical windings, capacitances and LC structures via coatings and electroplating. Multiple fabrications and tests were performed during the process, and the final result for the fabrication step was successful as it can be seen from this MRI image of the developed catheter tip.

The future work includes the combination of reliable FEM simulations which was studied in this thesis, and the developed catheter tip fabrication methods in order to create double tilted helix dependent or other form LC resonator structures as interventional 63.8 MHz MRI passive catheter devices. The planned structures will be first studied, 3D designed and simulated on FEM simulators to find the optimum solution from both dimensional and characteristics aspects. And following that, the fabrications, measurements and MRI tests will be carried out to materialize the designed structures. Obtaining a performance at the desired level, animal experiments will be performed to finalize the tests of catheter devices.

REFERENCES

1. Lauterbur, P. C., "Image Formation by Induced Local Interactions: Examples Employing Nuclear Magnetic Resonance", *Nature*, Vol. 242, No. 5394, pp. 190–191, 1973.

2. Garroway, A. N., P. K. Grannell and P. Mansfield, "Image Formation in NMR by a Selective Irradiative Process", *Journal of Physics C: Solid State Physics*, Vol. 7, No. 24, p. L457, 1974.

3. Kantor, H. L., R. W. Briggs and R. S. Balaban, "In Vivo 31P Nuclear Magnetic Resonance Measurements in Canine Heart Using a Catheter-Coil.", *Circulation Research*, Vol. 55, No. 2, pp. 261–266, 1984.

4. Hurst, G. C., J. Hua, J. L. Duerk and A. M. Cohen, "Intravascular (Catheter) NMR Receiver Probe: Preliminary Design Analysis and Application to Canine Iliofemoral Imaging", *Magnetic Resonance in Medicine*, Vol. 24, No. 2, pp. 343–357, 1992.

5. Martin, A. J., D. B. Plewes and R. M. Henkelman, "MR Imaging of Blood Vessels with an Intravascular Coil", *Journal of Magnetic Resonance Imaging*, Vol. 2, No. 4, pp. 421–429, 1992.

6. Nordbeck, P., W. R. Bauer, F. Fidler, M. Warmuth, K.-H. Hiller, M. Nahrendorf, M. Maxfield, S. Wurtz, W. Geistert and J. Broscheit, "Feasibility of Real-Time MRI with a Novel Carbon Catheter for Interventional Electrophysiology", *Circulation: Arrhythmia and Electrophysiology*, Vol. 2, No. 3, pp. 258–267, 2009.

7. Raval, A. N., J. D. Telep, M. a. Guttman, C. Ozturk, M. Jones, R. B. Thompson, V. J. Wright, W. H. Schenke, R. Desilva and R. J. Aviles, "Real-Time Magnetic Resonance Imaging–Guided Stenting of Aortic Coarctation with Commercially Available Catheter Devices in Swine", *Circulation*, Vol. 112, No. 5, pp. 699–706,

2005.

8. Kleinerman, R. A., "Cancer Risks Following Diagnostic and Therapeutic Radiation Exposure in Children", *Pediatric Radiology*, Vol. 36, No. 2, pp. 121–125, 2006.

9. Escaned, J., J. Goicolea, F. Alfonso, M. J. Perez-Vizcayno, R. Hernandez, A. Fernandez-Ortiz, C. BaÑUelos and C. Macaya, "Propensity and Mechanisms of Restenosis in Different Coronary Stent Designs: Complementary Value of the Analysis of the Luminal Gain-Loss Relationship", *Journal of the American College of Cardiology*, Vol. 34, No. 5, pp. 1490–1497, 1999.

10. Baptista, J., C. Di Mario, Y. Ozaki, J. Escaned, R. Gil, P. De Feyter, J. R. Roelandt and P. W. Serruys, "Impact of Plaque Morphology and Composition on the Mechanisms of Lumen Enlargement Using Intracoronary Ultrasound and Quantitative Angiography After Balloon Angioplasty", *The American Journal of Cardiology*, Vol. 77, No. 2, pp. 115–121, 1996.

11. Epstein, F. H., V. Fuster, L. Badimon, J. J. Badimon and J. H. Chesebro, "The Pathogenesis of Coronary Artery Disease and the Acute Coronary Syndromes", *New England Journal of Medicine*, Vol. 326, No. 4, pp. 242–250, 1992.

12. Quick, H. H., H. Kuehl, G. Kaiser, S. Bosk, J. F. Debatin and M. E. Ladd, "Inductively Coupled Stent Antennas in MRI", *Magnetic Resonance in Medicine*, Vol. 48, No. 5, pp. 781–790, 2002.

13. Beir, V., "Health Risks From Exposure to Low Levels of Ionizing Radiation", *Beir Vii Phase*, Vol. 2, 2006.

14. andreassi, M. G., L. Ait-Ali, N. Botto, S. Manfredi, G. Mottola and E. Picano, "Cardiac Catheterization and Long-Term Chromosomal Damage in Children with Congenital Heart Disease", *European Heart Journal*, Vol. 27, No. 22, pp. 2703–2708, 2006.

15. Omary, R. a., J. D. Green, B. E. Schirf, Y. Li, J. P. Finn and D. Li, "Real-Time Magnetic Resonance Imaging-Guided Coronary Catheterization in Swine", *Circulation*, Vol. 107, No. 21, pp. 2656–2659, 2003.

16. Kocaturk, O., C. E. Saikus, M. a. Guttman, A. Z. Faranesh, K. Ratnayaka, C. Ozturk, E. R. Mcveigh and R. J. Lederman, "Journal of Cardiovascular Magnetic Resonance", *Journal of Cardiovascular Magnetic Resonance*, Vol. 11, p. 29, 2009.

17. Formica, D. and S. Silvestri, "Biological Effects of Exposure to Magnetic Resonance Imaging: An Overview", *Biomedical Engineering Online*, Vol. 3, No. 1, p. 11, 2004.

18. Kanal, E., a. J. Barkovich, C. Bell, J. P. Borgstede, W. G. Bradley Jr, J. W. Froelich, T. Gilk, J. R. Gimbel, J. Gosbee and E. Kuhni-Kaminski, "ACR Guidance Document for Safe MR Practices: 2007", *American Journal of Roentgenology*, Vol. 188, No. 6, pp. 1447–1474, 2007.

19. Saikus, C. E. and R. J. Lederman, "Interventional Cardiovascular Magnetic Resonance Imaging: A New Opportunity for Image-Guided Interventions", *Jacc: Cardiovascular Imaging*, Vol. 2, No. 11, pp. 1321–1331, 2009.

20. Elgort, D. R., C. M. Hillenbrand, S. Zhang, E. Y. Wong, S. Rafie, J. S. Lewin and J. L. Duerk, "Image-Guided and-Monitored Renal Artery Stenting Using Only MRI", *Journal of Magnetic Resonance Imaging*, Vol. 23, No. 5, pp. 619–627, 2006.

21. Raman, V. K., P. V. Karmarkar, M. a. Guttman, A. J. Dick, D. C. Peters, C. Ozturk, B. S. Pessanha, R. B. Thompson, A. N. Raval and R. Desilva, "Real-Time Magnetic Resonance-Guided Endovascular Repair of Experimental Abdominal Aortic Aneurysm in Swine", *Journal of the American College of Cardiology*, Vol. 45, No. 12, pp. 2069–2077, 2005.

22. Raval, A. N., P. V. Karmarkar, M. a. Guttman, C. Ozturk, S. Sampath, R. Desilva, R. J. Aviles, M. Xu, V. J. Wright and W. H. Schenke, "Real-Time Magnetic Resonance Imaging–Guided Endovascular Recanalization of Chronic Total Arterial

Occlusion in a Swine Model", *Circulation*, Vol. 113, No. 8, pp. 1101–1107, 2006.

23. Buecker, A., E. Spuentrup, R. Grabitz, F. Freudenthal, E. G. Muehler, T. Schaeffter, J. J. Van Vaals and R. W. GÜNther, "Magnetic Resonance–Guided Placement of Atrial Septal Closure Device in Animal Model of Patent Foramen Ovale", *Circulation*, Vol. 106, No. 4, pp. 511–515, 2002.

24. Kuehne, T., S. Yilmaz, C. Meinus, P. Moore, M. Saeed, O. Weber, C. B. Higgins, T. Blank, E. Elsaesser and J. V. N. P. Y. P. Schnackenburg, Bernhard, "Magnetic Resonance Imaging-Guided Transcatheter Implantation of a Prosthetic Valve in Aortic Valve Position: Feasibility Study in Swine", .

25. Susil, R. C., C. J. Yeung, H. R. Halperin, A. C. Lardo and E. Atalar, "Multifunctional Interventional Devices for MRI: A Combined Electrophysiology/MRI Catheter", *Magnetic Resonance in Medicine*, Vol. 47, No. 3, pp. 594–600, 2002.

26. Dukkipati, S. R., R. Mallozzi, E. J. Schmidt, G. Holmvang, a. D'avila, R. Guhde, R. D. Darrow, G. Slavin, M. Fung and J. V. N. P. Y. P. Malchano, Zachary, "Electroanatomic Mapping of the Left Ventricle in a Porcine Model of Chronic Myocardial Infarction with Magnetic Resonance–Based Catheter Tracking", .

27. Krueger, S., O. Lips, B. David, D. Wirtz, S. Weiss, S. F. Pedersen, D. Caulfield, J. Bostock, R. Razavi and T. Schaeffter, "Towards Mr-Guided Ep Interventions Using an RF-Safe Approach", *Journal of Cardiovascular Magnetic Resonance*, Vol. 11, No. Suppl 1, pp. 1–3, 2009.

28. Sillerud, L. O., a. F. Mcdowell, N. L. Adolphi, R. E. Serda, D. P. Adams, M. J. Vasile and T. M. Alam, "1 H NMR Detection of Superparamagnetic Nanoparticles at 1t Using a Microcoil and Novel Tuning Circuit", *Journal of Magnetic Resonance*, Vol. 181, No. 2, pp. 181–190, 2006.

29. Rogers, J., R. J. Jackman and G. M. Whitesides, "Constructing Single-and Multiple-Helical Microcoils and Characterizing Their Performance As Compo-

nents of Microinductors and Microelectromagnets", *Microelectromechanical Systems, Journal of*, Vol. 6, No. 3, pp. 184–192, 1997.

30. Plewes, D. B. and W. Kucharczyk, "Physics of MRI: a Primer", *Journal of Magnetic Resonance Imaging*, Vol. 35, No. 5, pp. 1038–1054, 2012.

31. Rubin, D. L., A. V. Ratner and S. W. Young, "Magnetic Susceptibility Effects and Their Application in the Development of New Ferromagnetic Catheters for Magnetic Resonance Imaging.", *Investigative Radiology*, Vol. 25, No. 12, pp. 1325–1332, 1990.

32. Bakker, C. J., R. M. Hoogeveen, J. Weber, J. J. Van Vaals, M. a. Viergever and W. P. Mali, "Visualization of Dedicated Catheters Using Fast Scanning Techniques with Potential for Mr-Guided Vascular Interventions", *Magnetic Resonance in Medicine*, Vol. 36, No. 6, pp. 816–820, 1996.

33. Miquel, M. E., S. Hegde, V. Muthurangu, B. J. Corcoran, S. F. Keevil, D. L. Hill and R. S. Razavi, "Visualization and Tracking of an Inflatable Balloon Catheter Using Ssfp in a Flow Phantom and in the Heart and Great Vessels of Patients", *Magnetic Resonance in Medicine*, Vol. 51, No. 5, pp. 988–995, 2004.

34. Kozerke, S., S. Hegde, T. Schaeffter, R. Lamerichs, R. Razavi and D. L. Hill, "Catheter Tracking and Visualization Using 19f Nuclear Magnetic Resonance", *Magnetic Resonance in Medicine*, Vol. 52, No. 3, pp. 693–697, 2004.

35. Dharmakumar, R., I. Koktzoglou, R. Tang, K. R. Harris, N. Beohar and D. Li, "off-Resonance Positive Contrast Imaging of a Passive Endomyocardial Catheter in Swine", *Physics in Medicine and Biology*, Vol. 53, No. 13, p. N249, 2008.

36. Edelman, R. R., P. Storey, E. Dunkle, W. Li, a. Carrillo, A. Vu and T. J. Carroll, "Gadolinium-Enhanced off-Resonance Contrast Angiography", *Magnetic Resonance in Medicine*, Vol. 57, No. 3, pp. 475–484, 2007.

37. Krueger, S., S. Schmitz, S. Weiss, D. Wirtz, M. Linssen, H. Schade, N. Kraemer, E. Spuentrup, G. Krombach and A. Buecker, "An Mr Guidewire Based on Micropultruded Fiber-Reinforced Material", *Magnetic Resonance in Medicine*, Vol. 60, No. 5, pp. 1190–1196, 2008.

38. Mekle, R., E. Hofmann, K. Scheffler and D. Bilecen, "A Polymer-Based Mr-Compatible Guidewire: a Study to Explore New Prospects for Interventional Peripheral Magnetic Resonance Angiography (Ipmra)", *Journal of Magnetic Resonance Imaging*, Vol. 23, No. 2, pp. 145–155, 2006.

39. Bell, J. a., C. E. Saikus, K. Ratnayaka, V. Wu, M. Sonmez, A. Z. Faranesh, J. H. Colyer, R. J. Lederman and O. Kocaturk, "A Deflectable Guiding Catheter for Real-Time MRI-Guided Interventions", *Journal of Magnetic Resonance Imaging*, Vol. 35, No. 4, pp. 908–915, 2012.

40. Quick, H., M. Zenge, H. Kuehl, G. Kaiser, S. Aker, H. Eggebrecht, S. Massing and M. Ladd, "Wireless Active Catheter Visualization: Passive Decoupling Methods and Their Impact on Catheter Visibility", *13th Proceedings of the International Society for Magnetic Resonance in Medicine*, Vol. 2164, 2005.

41. Kuehne, T., R. Fahrig and K. Butts, "Pair of Resonant Fiducial Markers for Localization of Endovascular Catheters at All Catheter Orientations", *Journal of Magnetic Resonance Imaging*, Vol. 17, No. 5, pp. 620–624, 2003.

42. Quick, H. H., M. O. Zenge, H. Kuehl, G. Kaiser, S. Aker, S. Massing, S. Bosk and M. E. Ladd, "Interventional Magnetic Resonance Angiography with No Strings Attached: Wireless Active Catheter Visualization", *Magnetic Resonance in Medicine*, Vol. 53, No. 2, pp. 446–455, 2005.

43. Eggers, H., S. Weiss, P. Boernert and P. Boesiger, "Image-Based Tracking of Optically Detunable Parallel Resonant Circuits", *Magnetic Resonance in Medicine*, Vol. 49, No. 6, pp. 1163–1174, 2003.

44. Wong, M., Q. Zhang, J. Duerk, M. Lewin and M. Wendt, "An Optical System for Wireless Detuning of Parallel Resonant Circuits", *Journal of Magnetic Resonance Imaging*, Vol. 12, No. 4, pp. 632–638, 2000.

45. Celik, H., A. Ulutürk, T. Talı and E. Atalar, "A Catheter Tracking Method Using Reverse Polarization for Mr-Guided Interventions", *Magnetic Resonance in Medicine*, Vol. 58, No. 6, pp. 1224–1231, 2007.

46. Dumoulin, C., S. Souza and R. Darrow, "Real-Time Position Monitoring of Invasive Devices Using Magnetic Resonance", *Magnetic Resonance in Medicine*, Vol. 29, No. 3, pp. 411–415, 1993.

47. Ocali, O. and E. Atalar, "Intravascular Magnetic Resonance Imaging Using a Loopless Catheter Antenna", *Magnetic Resonance in Medicine*, Vol. 37, No. 1, pp. 112–118, 1997.

48. Kocaturk, O., A. H. Kim, C. E. Saikus, M. a. Guttman, A. Z. Faranesh, C. Ozturk and R. J. Lederman, "Active Two-Channel 0.035″ Guidewire for Interventional Cardiovascular MRI", *Journal of Magnetic Resonance Imaging*, Vol. 30, No. 2, pp. 461–465, 2009.

49. Pictet, J., R. Meuli, S. Wicky and J. J. Van Der Klink, "Radiofrequency Heating Effects Around Resonant Lengths of Wire in MRI", *Physics in Medicine and Biology*, Vol. 47, No. 16, p. 2973, 2002.

50. Ladd, M. E. and H. H. Quick, "Reduction of Resonant RF Heating in Intravascular Catheters Using Coaxial Chokes", *Magnetic Resonance in Medicine*, Vol. 43, No. 4, pp. 615–619, 2000.

51. Weiss, S., P. Vernickel, T. Schaeffter, V. Schulz and B. Gleich, "Transmission Line for Improved RF Safety of Interventional Devices", *Magnetic Resonance in Medicine*, Vol. 54, No. 1, pp. 182–189, 2005.

52. Schenck, J. F., "The Role of Magnetic Susceptibility in Magnetic Resonance Imaging: MRI Magnetic Compatibility of the First and Second Kinds", *Medical Physics*, Vol. 23, No. 6, pp. 815–850, 1996.

53. Barker, G., a. Simmons, S. Arridge and P. Tofts, "A Simple Method for Investigating the Effects of Non-Uniformity of Radiofrequency Transmission and Radiofrequency Reception in MRI.", *The British Journal of Radiology*, Vol. 71, No. 841, pp. 59–67, 1998.

54. Van Bentum, P., J. Janssen and A. Kentgens, "Towards Nuclear Magnetic Resonance μ-Spectroscopy and μ-Imaging", *Analyst*, Vol. 129, No. 9, pp. 793–803, 2004.

55. G Webb, a., "Radiofrequency Microcoils in Magnetic Resonance", *Progress in Nuclear Magnetic Resonance Spectroscopy*, Vol. 31, No. 1, pp. 1–42, 1997.

56. Mohmmadzadeh, M., N. Baxan, V. Badilita, K. Kratt, H. Weber, J. Korvink, U. Wallrabe, J. Hennig and D. Von Elverfeldt, "Characterization of a 3d Mems Fabricated Micro-Solenoid at 9.4 T", *Journal of Magnetic Resonance*, Vol. 208, No. 1, pp. 20–26, 2011.

57. Demas, V., A. Bernhardt, V. Malba, K. L. Adams, L. Evans, C. Harvey, R. S. Maxwell and J. L. Herberg, "Electronic Characterization of Lithographically Patterned Microcoils for High Sensitivity NMR Detection", *Journal of Magnetic Resonance*, Vol. 200, No. 1, pp. 56–63, 2009.

58. Goloshevsky, A., J. Walton, M. Shutov, J. De Ropp, S. Collins and M. Mccarthy, "Development of Low Field Nuclear Magnetic Resonance Microcoils", *Review of Scientific Instruments*, Vol. 76, No. 2, p. 024101, 2005.

59. Walton, J., J. De Ropp, M. Shutov, A. Goloshevsky, M. Mccarthy, R. Smith and S. Collins, "A Micromachined Double-Tuned NMR Microprobe", *Analytical Chemistry*, Vol. 75, No. 19, pp. 5030–5036, 2003.

60. Peck, T., R. Magin, J. Kruse and M. Feng, "NMR Microspectroscopy Using 100 Microns Planar RF Coils Fabricated on Gallium Arsenide Substrates.", *Ieee Transactions on Bio-Medical Engineering*, Vol. 41, No. 7, pp. 706–709, 1994.

61. Massin, C., G. Boero, F. Vincent, J. Abenhaim, P.-A. Besse and R. Popovic, "High-Q Factor RF Planar Microcoils for Micro-Scale NMR Spectroscopy", *Sensors and Actuators A: Physical*, Vol. 97, pp. 280–288, 2002.

62. Woytasik, M., J.-P. Grandchamp, E. Dufour-Gergam, J.-P. Gilles, S. Megherbi, E. Martincic, H. Mathias and P. Crozat, "Two-and Three-Dimensional Microcoil Fabrication Process for Three-Axis Magnetic Sensors on Flexible Substrates", *Sensors and Actuators A: Physical*, Vol. 132, No. 1, pp. 2–7, 2006.

63. Sillerud, L. O., a. F. Mcdowell, N. L. Adolphi, R. E. Serda, D. P. Adams, M. J. Vasile and T. M. Alam, "1 H NMR Detection of Superparamagnetic Nanoparticles at 1T Using a Microcoil and Novel Tuning Circuit", *Journal of Magnetic Resonance*, Vol. 181, No. 2, pp. 181–190, 2006.

64. Rogers, J., R. J. Jackman and G. M. Whitesides, "Constructing Single-and Multiple-Helical Microcoils and Characterizing Their Performance As Components of Microinductors and Microelectromagnets", *Microelectromechanical Systems, Journal of*, Vol. 6, No. 3, pp. 184–192, 1997.

65. Rogers, J. a., R. J. Jackman, G. M. Whitesides, D. L. Olson and J. V. Sweedler, "Using Microcontact Printing to Fabricate Microcoils on Capillaries for High Resolution Proton Nuclear Magnetic Resonance on Nanoliter Volumes", *Applied Physics Letters*, Vol. 70, No. 18, pp. 2464–2466, 1997.

66. Malba, V., R. Maxwell, L. B. Evans, A. F. Bernhardt, M. Cosman and K. Yan, "Laser-Lathe Lithography—A Novel Method for Manufacturing Nuclear Magnetic Resonance Microcoils", *Biomedical Microdevices*, Vol. 5, No. 1, pp. 21–27, 2003.

67. Jackson, D., C. Aracne-Ruddle, V. Malba, S. Weir, S. Catledge and Y. Vohra,

"Magnetic Susceptibility Measurements at High Pressure Using Designer Diamond Anvils", *Review of Scientific Instruments*, Vol. 74, No. 4, pp. 2467–2471, 2003.